



# Multiple perovskite layered lanthanum nickelate Ruddlesden-Popper systems as highly active bifunctional oxygen catalysts

Sung Ryul Choi<sup>a,1</sup>, John-In Lee<sup>a,1</sup>, Hyunyoung Park<sup>a</sup>, Sung Won Lee<sup>a</sup>, Dong Yeong Kim<sup>a</sup>, Won Young An<sup>a</sup>, Jung Hyun Kim<sup>b</sup>, Jongsoon Kim<sup>a,d</sup>, Hyun-Seok Cho<sup>c</sup>, Jun-Young Park<sup>a,\*</sup>

<sup>a</sup> HMC, Department of Nanotechnology and Advanced Materials Engineering, Sejong University, Seoul 05006, South Korea

<sup>b</sup> Department of Advanced Materials Science and Engineering, Hanbat National University, Daejeon 34158, South Korea

<sup>c</sup> New and Renewable Energy, Korea Institute of Energy Research, Daejeon 34129, South Korea

<sup>d</sup> Department of Energy Science, Sungkyunkwan University, Suwon 16419, Republic of Korea

## ARTICLE INFO

### Keywords:

Doped lanthanum nickelate  
Ruddlesden-Popper structure  
Bifunctional electrocatalyst  
Oxygen evolution reaction  
Oxygen reduction reaction  
Oxygen electrode activity

## ABSTRACT

A systematic study of the Ruddlesden-Popper structured  $\text{La}_{n+1}\text{Ni}_n\text{O}_{3n+1}$  ( $n = 1, 2, 3,$  and  $4$ ) and its catalytic performance in oxygen evolution (OER) and oxygen reduction reactions (ORR) is carried out with a view to design a highly-efficient and cost-effective electrocatalyst. In particular, we introduce for the first time a novel  $\text{La}_5\text{Ni}_4\text{O}_{13.8}$  with a 4-layered perovskite structure ( $n = 4$ ) for use as a highly active and durable bifunctional oxygen catalyst for OER/ORR. Concretely,  $\text{La}_5\text{Ni}_4\text{O}_{13.8}$  catalysts has demonstrated performance of 1.65 V at 10  $\text{mA}\cdot\text{cm}^{-2}$  and 0.66 V at near half-wave potential ( $-3 \text{ mA}\cdot\text{cm}^{-2}$ ) for OER and ORR, respectively, this indicates excellent intrinsic OER/ORR kinetics. Furthermore, by controlling the fuel-to-oxidizer ratio (using extremely fuel-rich conditions) in the glycine-nitrate combustion technique, the 4-layered perovskite  $\text{La}_5\text{Ni}_4\text{O}_{13.8}$  catalysts are synthesized as a single Ruddlesden-Popper phase with various dopants to further boost its bifunctional oxygen electrode activity. Among OER/ORR catalysts,  $\text{La}_5\text{Ni}_3\text{CoO}_{13.8}$  catalysts exhibit exceptional electrocatalytic activity with low overpotential and Tafel slope ( $35/76 \text{ mV}\cdot\text{dec}^{-1}$  for OER/ORR). Outstandingly, the  $\text{La}_5\text{Ni}_3\text{CoO}_{13.8}$  is able to achieve an extremely low overpotential of 370 mV at 10  $\text{mA}\cdot\text{cm}^{-2}$  in 0.1 M KOH for OER, surpassing Ir/C catalysts and any metal oxide catalyst ever reported. The high catalytic performance of  $\text{La}_5\text{Ni}_3\text{CoO}_{13.8}$  can be attributed to its favorable electronic structure enriched with oxygen defects and electronic charge carriers (increased Ni oxidation state) as well as to the promoted lattice-oxygen oxidation mechanism pathway that comes from strong metal-oxygen covalency (high oxygen-ion diffusion rate).

## 1. Introduction

The use of conventional fossil fuels to generate energy is having ever-increasing detrimental effects on the environment and climate, this problem has stimulated many comprehensive investigations and pieces of research to develop clean, renewable next-generation energy storage and conversion technologies [1,2]. Of utmost importance for the performance of these next-generation electrochemical energy devices are the quality of the oxygen reduction reactions (ORR) and oxygen evolution reactions (OER) that take place within them, these reactions have intrinsically sluggish kinetics due to multistep electron and ion transfers [3-5]. To date, precious metal-based electrocatalysts have been identified as the gold standard oxygen electrode catalysts, owing to their high

activity (for example, Pt/C for ORR and Ir/C for OER); however, the scarcity, high cost, and low bifunctionality of Pt/C and Ir/C have seriously impeded the worldwide commercial application of these devices [6]. Over the past few decades, nanostructured transition metal (e.g. Ni, Co, and Fe)-based oxides have emerged as promising candidates for this kind of catalyst due to their abundance, bifunctionality, and reasonable activities for both OER and ORR [7-9]. In particular, perovskite-structured oxides with a general formula of  $\text{ABO}_3$ , in which A is a rare-earth or alkaline earth material and B is a transition metal, can host a myriad of structures (single, double, and triple) and compositions created by substitution of ions of different radii and valences in the A and B-sites [10-14]. Nevertheless, perovskite oxide-based electrocatalysts have several major drawbacks: large overpotential for

\* Corresponding author.

E-mail address: [jyoung@sejong.ac.kr](mailto:jyoung@sejong.ac.kr) (J.-Y. Park).

<sup>1</sup> Sung Ryul Choi and John-In Lee contributed equally as first authors.

catalyzing OER/ORR and low mass activity that results from the small electrochemically active surface area. Hence, further advances in terms of activity and stability are still crucial for their use to become prevalent in next-generation energy storage and conversion technologies.

Recently, Suntivich *et al.* [15] proposed that catalytic activity for oxides is predominantly related to  $e_g$  ( $\sigma^*$ -orbital) occupation and the extent of B-site transition-metal–oxygen covalency. According to the volcano relationship that describes catalyst activity as dependent on  $e_g$  electron numbers, perovskite-structured  $\text{LaNiO}_3$  was expected to provide excellent OER/ORR electrocatalysts. More recently, there has been significant interest in La-Ni based layered perovskite compounds, these are classified as Ruddlesden–Popper-type oxides with the formula  $\text{La}_{n+1}\text{Ni}_n\text{O}_{3n+1}$  [16–19]. The Ruddlesden–Popper structured materials,  $\text{La}_{n+1}\text{Ni}_n\text{O}_{3n+1}$ , are composed of perovskite ( $\text{LaNiO}_3$ ) layers inserted between two Rocksalt layers (LaO), stacking along the *c*-axis [20–23]. Shao *et al.* [24] conducted a systematic study on the OER/ORR performances of  $\text{La}_{n+1}\text{Ni}_n\text{O}_{3n+1}$  (LNO,  $n = 1, 2, \text{ and } 3$ ) and discovered that the catalytic activity of LNO is dependent on the  $n$  value at room temperature in alkaline medium. However, the case of  $n > 3$  ( $3 < n < \infty$ ) has not been reported yet, despite the fact that the  $n$  value significantly influences the electrocatalytic properties of Ruddlesden–Popper LNO during OER/ORR. This may be because conventional solid-state techniques have only been successful in making polycrystalline samples with  $n = 1–3$  [25,26]. Moreover, the doping effect of LNO in La and Ni-sites on the electrocatalytic performances has not been studied systematically because of the technical difficulties in synthesizing single Ruddlesden–Popper  $\text{La}_{n+1}\text{Ni}_n\text{O}_{3n+1}$  phases with various dopants.

Herein, we report on transition metal ( $M = \text{Fe, Co}$ )-doped  $\text{La}_{n+1}\text{Ni}_n\text{M}_x\text{O}_{3n+1}$  (LNM- $x$ ,  $n = 1, 2, 3$ , and  $4$ ,  $x = 0.5, 1.0, 1.5$ , and  $2.0$ ) with  $n$  layered perovskite structures that are highly active for OER/ORR in alkaline medium. The  $n$  layered perovskite LNM catalysts are synthesized using glycine-nitrate combustion (GNC) techniques [27–29]. By controlling the fuel-to-oxidizer ratio (to extremely fuel-rich conditions) during the GNC technique, the 4-layered perovskite LNM catalysts can be synthesized as a single Ruddlesden–Popper phase with various dopants. Benefiting from  $n$  layered perovskite structures with transition metal dopants,  $\text{La}_5\text{Ni}_3\text{CoO}_{13.8}$  (LNC-1.0) catalysts exhibit outstanding bifunctional electrocatalytic activity for OER/ORR with low overpotential and Tafel slope ( $35/76 \text{ mV}\cdot\text{dec}^{-1}$ ). Their oxygen electrode activity [ $\Delta E = E_{\text{OER}} (\text{at } 10 \text{ mA}\cdot\text{cm}^{-2}) - E_{\text{ORR}} (-3 \text{ mA}\cdot\text{cm}^{-2})$ ] is as small as  $0.942 \text{ V}$ , which is comparable to any metal oxide catalyst ever reported [30–32]. The high catalytic performance from LNC-1.0 is attributed to its favorable electronic structure that is enriched with oxygen defects and electronic charge carriers (increased Ni oxidation state) as well as the promoted lattice-oxygen oxidation mechanism pathway that comes from strong metal–oxygen covalency (high oxygen-ion diffusion rate) [33–36].

## 2. Experimental

### 2.1. Synthesis of multiple perovskite layered lanthanum nickelate systems

The Ruddlesden–Popper  $\text{La}_{n+1}\text{Ni}_n\text{O}_{3n+1}$  (LNO,  $n = 1, 2, 3$ , and  $4$ ) family of catalysts were synthesized through a glycine nitrate combustion (GNC) process. To prepare LNO electrocatalysts, stoichiometric amounts of lanthanum nitrate hexahydrate [ $\text{La}(\text{NO}_3)_3\cdot 6\text{H}_2\text{O}$ , 98% purity, Alfa Aesar], nickel nitrate hexahydrate [ $\text{Ni}(\text{NO}_3)_2\cdot 6\text{H}_2\text{O}$ , 98% purity, Alfa Aesar] were mixed with glycine ( $\text{NH}_2\text{CH}_2\text{COOH}$ ) as the fuel in deionized water. In order to drive the combustion reaction with the maximum energy, a high glycine to nitrate molar ratio of 8.5 was used, this allowed us to synthesize high numbers of perovskite layers in the Ruddlesden–Popper structure. The mixture was then heated to  $300^\circ\text{C}$  while stirring with a magnetic bar (120 rpm) to form a homogeneous suspension. After auto-ignition of the mixture, the ashes were collected, ground with a mortar and pestle, and then calcined at  $1100^\circ\text{C}$  for 5 h to obtain the Ruddlesden–Popper structure LNO powders.

The Ni-site transition metal ( $M = \text{Fe, Co}$ )-doped  $\text{La}_5\text{Ni}_{4-x}\text{M}_x\text{O}_{13.8}$  ( $x = 0.5, 1.0, 1.5$ , and  $2.0$ ) catalysts were also prepared using the GNC process. Iron nitrate nonahydrate [ $\text{Fe}(\text{NO}_3)_3\cdot 9\text{H}_2\text{O}$ , 98% purity, Alfa Aesar], Cobalt nitrate hexahydrate [ $\text{Co}(\text{NO}_3)_2\cdot 6\text{H}_2\text{O}$ , 98% purity, Alfa Aesar], lanthanum nitrate hexahydrate [ $\text{La}(\text{NO}_3)_3\cdot 6\text{H}_2\text{O}$ , 98% purity, Alfa Aesar], nickel nitrate hexahydrate [ $\text{Ni}(\text{NO}_3)_2\cdot 6\text{H}_2\text{O}$ , 98% purity, Alfa Aesar] were dissolved with glycine in deionized water. The solution was mixed with a magnetic bar and slowly dehydrated at  $300^\circ\text{C}$  until the auto-combustion of the precursors. The ashes were ground and then calcined at  $1100^\circ\text{C}$  for 5 h.

### 2.2. Characterization of layered lanthanum nickelate systems

Crystalline structures of the catalysts were determined by X-ray diffraction (XRD, Rigaku D/MAX 2500 Diffractometer) with filtered  $\text{Cu K}\alpha$  radiation ( $\lambda = 1.5444 \text{ \AA}$ ). The XRD data was collected by step scanning in the  $2\theta$  range of  $20–80^\circ$  with intervals of  $0.02^\circ$ . Each X-ray diffractogram was refined by profile matching using the Fullprof software and Rietveld structural refinements were then conducted to determine the crystal structure parameters (atom coordinates and lattice parameters). The chemical state and electronic structure of the catalysts were identified by X-ray photoelectron spectroscopy (XPS, VG Escalab 220i, UK) using a monochromatic Al  $\text{K}\alpha$  X-ray source ( $h\nu = 1,486.6 \text{ eV}$ ). Relative atomic concentrations were compared using the peak intensities of Ni  $2p$  and O  $1s$  of the catalysts, normalized to their ionization cross-sections.

The morphology of the catalysts was examined by field emission scanning electron microscopy (FESEM, S-4700 Hitachi, acceleration voltage of  $15 \text{ kV}$ ) and high resolution transmission electron microscopy (HRTEM, JEM-F200, JEOL, acceleration voltage of  $200 \text{ kV}$ ). Corresponding energy-dispersive X-ray spectroscopy (EDX) elemental mapping images of the component phases were taken with an Oxford instruments device the FESEM was equipped with. Electrocatalysts were dispersed in ethanol by sonication to prepare specimens for FESEM and HRTEM. The Brunauer–Emmet–Teller (BET) surface area catalysts were analyzed using  $\text{N}_2$  adsorption/desorption medium (BELSORP-max, BEL) at  $77 \text{ K}$  after drying the samples for 3 h at  $250^\circ\text{C}$ , their pore size distributions were calculated by the Barrett–Joyner–Halenda (BJH) method from the adsorption branches of the isotherms.

### 2.3. Electrochemical measurements of layered lanthanum nickelate systems

Electrochemical analysis of the bifunctional OER and ORR catalysts was performed on a rotating disk electrode (RDE) system (RRDE-3A, ALS) at room temperature. Catalyst inks were prepared by dispersing  $10 \text{ mg}$  of the catalyst powder and  $5 \text{ mg}$  of conductive carbon (Vulcan XC-72R, Cabot) in  $16 \mu\text{L}$  aqueous Nafion solution (Sigma-Aldrich),  $250 \mu\text{L}$  of isopropanol, and  $750 \mu\text{L}$  of deionized water, this was followed by bath sonication for 30 min. A  $1 \mu\text{L}$  catalyst slurry was drop-cast onto a glassy carbon disk electrode (diameter of  $3 \text{ mm}$  and  $0.07069 \text{ cm}^2$  electrode area) and dried at room temperature to form a uniform thin film working electrode. Electrochemical testing was performed in a standard three-electrode cell using a Pt wire counter electrode, an Hg/HgO (sat.  $1 \text{ M NaOH}$ ) reference electrode, and the as-prepared catalyst coated glassy carbon working electrode. All potentials reported in this study were converted to the reversible hydrogen electrode (RHE) scale, unless otherwise specified. All electrochemical experiments were conducted on a potentiostat/galvanostat electrochemical analyzer (SP-150, Biologic, France).

Cyclic voltammetry (CV) scans were performed between  $0.05$  and  $1.2 \text{ V}$  for 50 cycles (scan rate of  $100 \text{ mV}\cdot\text{s}^{-1}$ ) to clean the surface of the catalyst before electrochemical tests. For OER activity measurements, the CV was obtained in  $\text{O}_2$ -saturated  $0.1 \text{ M KOH}$  electrolyte solution at a scan rate of  $5 \text{ mV}\cdot\text{s}^{-1}$  ( $1,600 \text{ rpm}$ ) between  $1.2$  and  $1.7 \text{ V}$ . Overpotentials were obtained by subtracting the thermodynamic potential for water

oxidation from the measured potential at a current density of 5 and 10  $\text{mA}\cdot\text{cm}^{-2}$ . ORR activity measurements were conducted in an  $\text{O}_2$ -saturated 0.1 M KOH solution by LSV from 1.2 to 0.2 V at a scan rate of  $5\text{ mV}\cdot\text{s}^{-1}$  (rotating speeds of 400, 900, 1,600, and 2,500 rpm). To compensate for the effect of solution resistance, all the potentials are  $iR$ -corrected potentials ( $=E-iR$  where  $i$  is the current density and  $R$  is the uncompensated ohmic electrolyte resistance recorded via SP-150 electrochemical impedance spectroscopy (EIS, BioLogic). EIS measurements were carried out in the frequency range of 100 kHz – 100 mHz. The AC amplitude was set at 10 mV. The resistance components of catalysts were separated as the ohmic ( $R_{\text{ohmic}}$ ), charge-transport ( $R_{\text{ct}}$ ), and mass-transport resistances ( $R_{\text{m}}$ ) from the fitted equivalent circuit using EC-Lab software.

The potential difference between the OER and ORR characteristics was calculated to assess the comprehensive oxygen electrode activity of the catalysts. Electrochemical active surface area (ECSA) of the catalysts was estimated by dividing the double-layer capacitances ( $C_{\text{dl}}$ ) by the specific capacitance ( $C_s \approx 40\ \mu\text{F}\cdot\text{cm}^{-2}$ ). ECSA tests were carried out under the potential window of 0.1–0.2 V (vs. RHE) with different scan rates of 10, 20, 50, 100, 150, and 200  $\text{mV}\cdot\text{s}^{-1}$ . Durability was evaluated by LSV curves under a potential sweep of 1.25–1.65 V for 1,000 cycles (scan rate of  $200\text{ mV}\cdot\text{s}^{-1}$ ) for OER and a sweep of 0.6–1.1 V for 10,000 cycles (scan rate of  $200\text{ mV}\cdot\text{s}^{-1}$ ) for ORR. The oxygen intercalation and diffusion coefficient measurements were performed in an  $\text{N}_2$ -saturated 1 M KOH aqueous solution at a scan rate of  $20\text{ mV}\cdot\text{s}^{-1}$  (GC working electrode, Pt wire counter electrode, and Hg/HgO reference electrode) [36]. Chronoamperometry experiments were performed by applying a 50 mV more anodic of the halfway potential between the peak currents for oxygen insertion and extraction at 2000 rpm rotation rate. The oxygen ion diffusion coefficient ( $D_{\text{O}}$ ) was calculated by the equation  $\lambda = a(D_{\text{O}}t)^{-1/2}$ , where  $\lambda$  dimensionless shape factor [assumed to be 2, estimated the values from a sphere (1.77) and cube (2.26)] and  $a$  is the radius of the particles (obtained from the measurement of radius by SEM

images), using a bounded three-dimensional diffusion model [35–37].

### 3. Results and discussion

#### 3.1. Structural and microstructural characterizations of catalysts

Crystalline structures of the synthesized Ruddlesden-Popper  $\text{La}_{n+1}\text{Ni}_n\text{O}_{3n+1}$  (LNO,  $n = 1, 2, 3,$  and  $4$ ) family of catalysts were investigated by x-ray diffraction (XRD). Fig. 1a shows the XRD patterns of the  $\text{La}_{n+1}\text{Ni}_n\text{O}_{3n+1}$  materials, as well as their Rietveld refinement results. The XRD patterns of the  $\text{La}_2\text{NiO}_{4+\delta}$  (L2N1),  $\text{La}_3\text{Ni}_2\text{O}_{7-\delta}$  (L3N2),  $\text{La}_4\text{Ni}_3\text{O}_{10-\delta}$  (L4N3), and  $\text{La}_5\text{Ni}_4\text{O}_{13-\delta}$  (L5N4) powders show the formation of the Ruddlesden-Popper  $\text{K}_2\text{NiF}_4$  structure (inorganic crystal structure data, ICSD, no. 39004) free of any undesirable phases (For your information, L5N4 was not yet recorded in the ICSD) [38]. The crystal structures (space group) of L2N1 was identified as tetragonal ( $I/4mmm$ ), while L3N2, L4N3, and L5N4 were indexed with the tetragonal ( $Fmmm$ ) phase [16,24,39]. The Ruddlesden-Popper structured LNO consists of alternating rock-salt layers ( $\text{LaO}$ ) and perovskite layers ( $\text{LaNiO}_3$ ) $_n$  along the crystallographic  $c$  direction, as shown in Fig. 1b. The lattice constants of the Ruddlesden-Popper structured catalysts calculated using the Rietveld refinements were comparatively invariant for  $a$ - and  $b$ -axes. The lattice parameters,  $a$  (and  $b$ ) of L2N1, L3N2, L4N3, and L5N4 were 3.8625 (3.8625), 5.3993 (5.4468), 5.4147 (5.4601), and 5.4184 Å (5.4635 Å), respectively (Table 1). On the other hand, the  $c$ -axis lattice constants of the catalysts showed remarkable differences, they progressively increased from 12.6916 Å to 20.4778, to 28.0081, and to 35.9460 Å for L2N1, L3N2, L4N3, and L5N4, respectively, this demonstrates the formation of higher order Ruddlesden-Popper phases with increasing  $n$  (=the number of perovskite layers) in this structure.

Size and morphology of the LNO catalysts were investigated by FESEM and HRTEM. The LNO particles synthesized with the glycine-nitrate combustion method show an agglomerated sheet-like grain

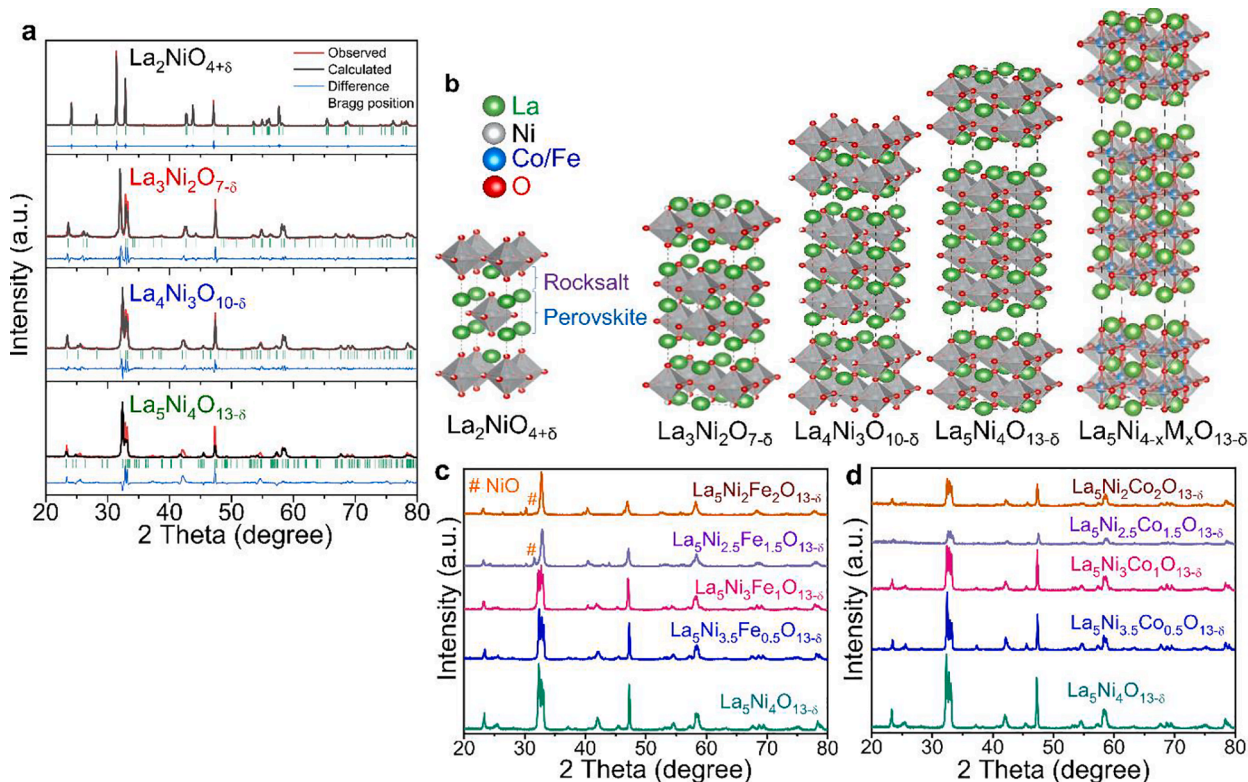


**Fig. 1.** (a) XRD diffraction patterns with their Rietveld refinement results for as-synthesized Ruddlesden-Popper structured catalysts. (b) Crystalline structure of  $\text{La}_2\text{NiO}_{4+\delta}$ ,  $\text{La}_3\text{Ni}_2\text{O}_{7-\delta}$ ,  $\text{La}_4\text{Ni}_3\text{O}_{10-\delta}$ ,  $\text{La}_5\text{Ni}_4\text{O}_{13-\delta}$ , and  $\text{La}_5\text{Ni}_{4-x}\text{M}_x\text{O}_{13-\delta}$  ( $M = \text{Co}, \text{Fe}$ ). (c) XRD patterns of as-synthesized  $\text{La}_5\text{Ni}_{4-x}\text{Fe}_x\text{O}_{13-\delta}$  ( $x = 0, 0.5, 1.0, 1.5,$  and  $2.0$ ). (d) XRD patterns of as-synthesized  $\text{La}_5\text{Ni}_{4-x}\text{Fe}_x\text{O}_{13-\delta}$  ( $x = 0, 0.5, 1.0, 1.5,$  and  $2.0$ ) catalysts.

**Table 1**

Lattice parameters and structural information for  $\text{La}_{n+1}\text{Ni}_n\text{O}_{3n+1}$  ( $n = 1, 2, 3, \text{ and } 4$ ),  $\text{La}_5\text{Ni}_3\text{FeO}_{13-6}$ , and  $\text{La}_5\text{Ni}_3\text{CoO}_{13-6}$  from Rietveld refinement and chemical titration method.

Catalysts	Space group(phase structure)	Lattice parameter / nm			$c/a$	Oxygen non-stoichiometry	Reliability factors ( $R_p, \chi^2$ )
		$a$	$b$	$c$			
$\text{La}_2\text{NiO}_{4-6}$	$I4/mmm(\text{Tetragonal})$	3.8625	3.8625	12.6916	3.286	0.08	5.39%, 2.41
$\text{La}_3\text{Ni}_2\text{O}_{7-6}$	$Fm\bar{3}m(\text{Tetragonal})$	5.3993	5.4468	20.4778	3.793	0.05	9.44%, 7.92
$\text{La}_4\text{Ni}_3\text{O}_{10-6}$		5.4147	5.4601	28.0081	5.173	0.13	8.40%, 4.93
$\text{La}_5\text{Ni}_4\text{O}_{13-6}$		5.4184	5.4635	35.9460	6.634	0.21	16.0%, 23.2

morphology with diameters of 50–250 nm, this is a typical shape for layered structure materials and is caused by a buildup of layers along the  $c$ -axis (Fig. 2 and S1) [40]. Elemental mapping images of LNO based on SEM/EDX show that the constituent elements (La, Ni, and O) are uniformly distributed without any observable elemental segregation. Table 2 summarizes the elemental composition of the LNO samples derived from the EDX analysis. The relative atomic percentages of lanthanum and nickel are 2:1.0, 3:1.8, 4:3.1, and 5:4.2 for L2N1, L3N2, L4N3, and L5N4, respectively, this confirms that lanthanum and nickel were well synthesized at the desired ratio in the Ruddlesden-Popper LNO structure. The Ruddlesden-Popper structure in the LNO was further confirmed by the selected area electron diffraction (SAED) pattern from the HRTEM image (Fig. 2g and S2). The inset of Fig. 2g shows the representative points in the SAED pattern, these can be indexed as (020) and (0010) reflections along the [100] zone axis of the LNO. A well-organized arrangement of stacking layers of  $\text{LaO}(\text{LaNiO}_3)_4$  along the  $c$ -axis was observed. The repeated  $\text{LaO}$  layers along the  $c$ -axis were separated by 35.91 Å as seen in the enlarged image for L5N4, this is in agreement with the results obtained from the Rietveld refinement (Table 1). Fig. 3 shows nitrogen adsorption–desorption isotherms and pore size distribution curves of all the LNO electrocatalysts. All LNO samples showed similar BET surface areas of 0.85, 0.74, 0.80, and 0.77  $\text{m}^2\text{g}^{-1}$  for L2N1, L3N2, L4N3, and L5N4, respectively (Table 2). The catalysts pore size distributions were calculated from adsorption-desorption isotherms, these exhibit type IV shapes with mesoporous features (mean pore diameter of 9.1–12.9 nm).

### 3.2. Electrochemical activity and stability of catalysts

To investigate OER catalytic activity of the LNO catalysts, CV measurements were performed in an  $\text{O}_2$ -saturated 0.1 M KOH solution at a rotating speed of 1600 rpm and a scan rate of 5  $\text{mV}\cdot\text{s}^{-1}$  on RDE. As seen in Fig. 4a, OER activity of the LNO increased with the number of perovskite layers ( $n$ ) in the Ruddlesden-Popper structure and thus L5N4 exhibits better OER activity with a lower overpotential of 430 mV than the other catalysts. More specifically, the overpotential ( $\eta$ ) at 5  $\text{mA}\cdot\text{cm}^{-2}$  increased in the order: L5N4 (1.62 V), L4N3 (1.65 V), L3N2 (1.67 V), and L2N1 (1.68 V). To find the kinetic parameters of the LNO electrocatalysts, Tafel plots derived from polarization curves (negative scan of

**Table 2**

Characterization data for catalysts from  $\text{N}_2$  adsorption analysis and FESEM/EDX elemental mapping.

Catalysts	BET analysis		Elemental composition/EDX			
	BET surface area ( $\text{m}^2\cdot\text{g}^{-1}$ )	Mean pore diameter (nm)	La (%)	Ni (%)	La: Ni	Co or Fe (%)
$\text{La}_2\text{NiO}_{4-6}$	0.85	9.1	13.5	7.0	2:1.0	
$\text{La}_3\text{Ni}_2\text{O}_{7-6}$	0.74	12.8	13.6	8.2	3:1.8	
$\text{La}_4\text{Ni}_3\text{O}_{10-6}$	0.80	12.3	14.0	10.9	4:3.1	
$\text{La}_5\text{Ni}_4\text{O}_{13-6}$	0.77	12.9	9.5	8.0	5:4.2	
$\text{La}_5\text{Ni}_{3.5}\text{Fe}_{0.5}\text{O}_{13-6}$	1.22	9.1	19.1	12.0	5:3.1	1.9 (Fe)
$\text{La}_5\text{Ni}_3\text{CoO}_{13-6}$	0.85	16.4	13.1	7.2	5:2.8	2.6 (Co)

the CV curves), ohmic resistance-corrected potential ( $E-ir$ ) vs.  $\log j$  for OER were produced, these are shown in Fig. 4b. The Tafel slopes of L5N4, L4N3, L3N2, and L2N1 for OER were 70, 77, 87, and 114  $\text{mV}\cdot\text{dec}^{-1}$ , respectively, indicating the excellent OER kinetics of L5N4 (Table 3).

Fig. 4c represents the mass activity (normalized to the mass loading) and specific activity (normalized to the surface area from BET measurements) of the LNO electrocatalysts at  $\eta = 450$  mV (1.68 V vs. RHE) to evaluate the potential for scalability of water-splitting catalysts [41]. The L5N4 electrocatalyst exhibits a mass activity of 139  $\text{A}\cdot\text{g}^{-1}$ , which is  $\sim 3.2$  and  $3.6$  times that of the L3N2 and L2N1 electrocatalysts, respectively, indicating that this catalyst makes applicable in scaling-up of water electrolysis. It is well known that the specific activity also reveals the intrinsic OER activity of catalysts. The intrinsic activity of the catalysts for OER followed the order from worst to best of L2N1 ( $4.55 \text{ mA}\cdot\text{cm}^{-2}_{\text{BET}} < \text{L3N2}$  ( $5.95 \text{ mA}\cdot\text{cm}^{-2}_{\text{BET}} < \text{L4N3}$  ( $8.18 \text{ mA}\cdot\text{cm}^{-2}_{\text{BET}} < \text{L5N4}$  ( $18.2 \text{ mA}\cdot\text{cm}^{-2}_{\text{BET}}$ ), indicating the excellent intrinsic activity of high  $n$  value Ruddlesden-Popper structure electrocatalysts. Long-term OER stability of the synthesized catalysts was evaluated by potential cycling tests between 1.25 and 1.65 V (vs. RHE, scan rate of 5  $\text{mV}\cdot\text{s}^{-1}$ ) in an  $\text{O}_2$  saturated 0.1 M KOH solution at 1,600 rpm. Fig. 4d shows OER activity of L5N4 before and after the durability test. The potential difference of L5N4 at 10  $\text{mA}\cdot\text{cm}^{-2}$  was decreased by 6 mV after 1,000 cycles, demonstrating the high stability of L5N4 electrocatalyst during OER.

The ORR activities of the LNO electrocatalysts were also quantified by using a RDE in an  $\text{O}_2$ -saturated 0.1 M KOH solution. The linear sweep voltammetry (LSVs) measurements were taken at a rotation speed of 1600 rpm and a scan rate of 5  $\text{mV}\cdot\text{s}^{-1}$ , these are depicted in Fig. 5a. L5N4 shows better ORR activity with lower overpotential than the other catalysts. Onset potentials obtained from the LSV curves of L5N4, L4N3, L3N2, and L2N1 were 0.760, 0.732, 0.729, and 0.713 V, respectively. In addition, the half-wave potentials of L5N4, L4N3, L3N2, and L2N1 were 0.664, 0.650, 0.645, and 0.617 V, respectively. Catalytic activities of the LNO catalysts were also investigated using the Tafel plots in ORR polarization curves (Fig. 5b). The Tafel slopes of L5N4, L4N3, L3N2, and L2N1 for ORR were 90, 121, 136, and 167  $\text{mV}\cdot\text{dec}^{-1}$ , respectively, indicating the excellent ORR kinetics of L5N4 (Table 3). Additionally, the unique L5N4 catalyst achieved an ORR mass activity of 10.1  $\text{A}\cdot\text{g}^{-1}$  and a specific activity of 1.32  $\text{mA}\cdot\text{cm}^{-2}_{\text{BET}}$ , these are the highest among all the test samples, at 0.7 V vs. RHE (Fig. 5c).

The inverse measured current density ( $j^{-1}$ ) was plotted vs. inverse square root of the rotation speed ( $\omega$ ) at 0.4–0.7 V by Koutecky-Levich analysis. In the Koutecky-Levich plot (Fig. 5d), L5N4 exhibited linear increases in inverse measured current density with increasing values of the inverse square root of the rotation speed, this reveals the first-order electrochemical reaction kinetics toward dissolved oxygen [42]. Transferred electron numbers per oxygen molecule calculated by the empirical Koutecky-Levich equation for L2N1, L3N2, L4N3, and L5N4 were 2.1, 2.3, 2.8, and 3.6, respectively, this implies that the 4-electron process of the LNO catalysts can be used as a gauge for high ORR catalytic activity. For long-term ORR stability testing, the LNO electrocatalysts were cycled between 0.6 and 1.1 V (vs. RHE) for 10,000 cycles in a 0.1 M  $\text{O}_2$ -saturated KOH solution at 1600 rpm. As shown in Fig. 5e, L5N4 exhibits a decline in ORR activity of 37 mV at  $-3 \text{ mA}\cdot\text{cm}^{-2}$ .

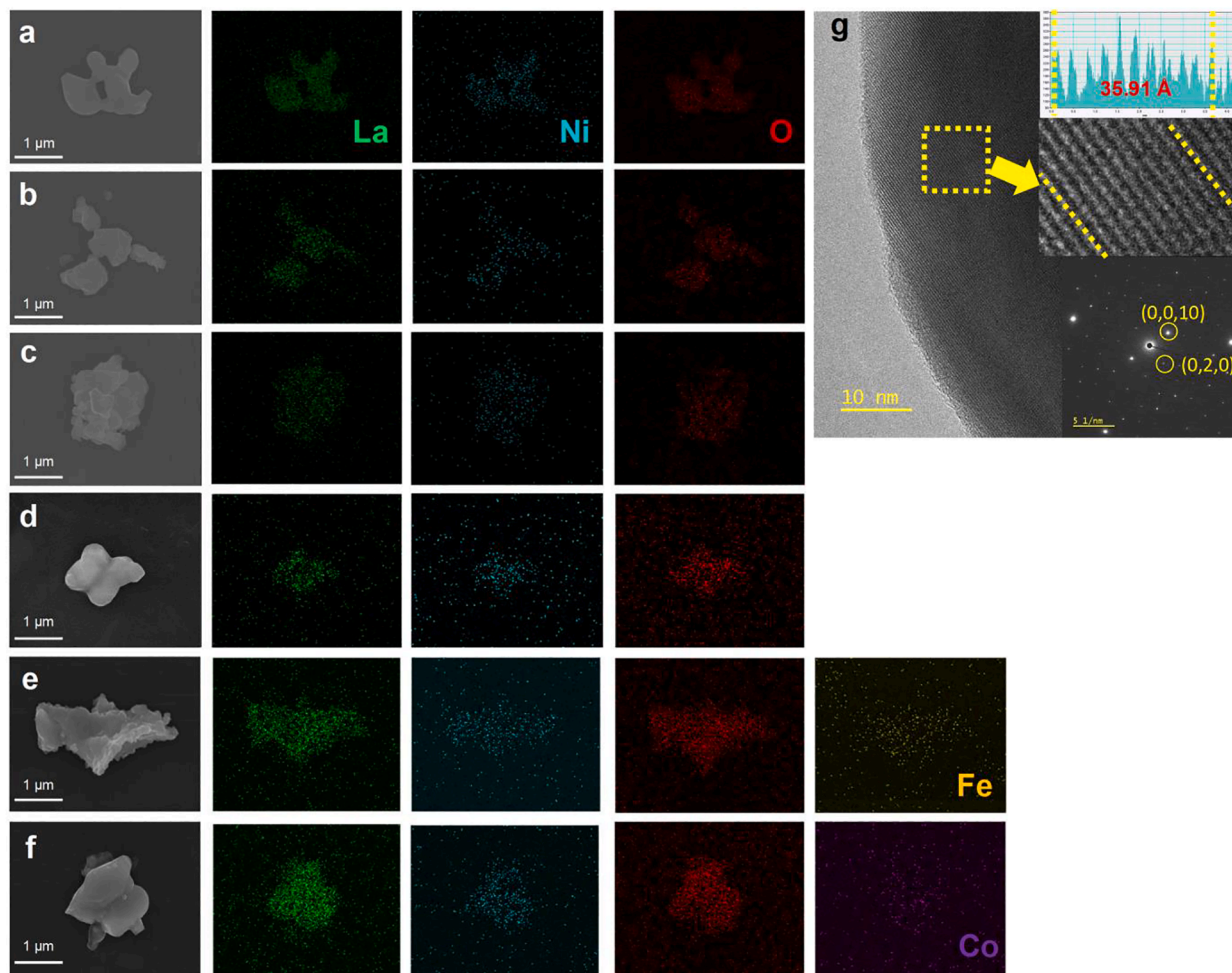


**Fig. 2.** FESEM images and EDX elemental mapping results for (a) La<sub>2</sub>NiO<sub>4+6</sub>, (b) La<sub>3</sub>Ni<sub>2</sub>O<sub>7-6</sub>, (c) La<sub>4</sub>Ni<sub>3</sub>O<sub>10-6</sub>, (d) La<sub>5</sub>Ni<sub>4</sub>O<sub>13-6</sub>, (e) La<sub>5</sub>Ni<sub>3.5</sub>Fe<sub>0.5</sub>O<sub>13-6</sub>, and (f) La<sub>5</sub>Ni<sub>4</sub>Co<sub>1</sub>O<sub>13-6</sub>. (g) HRTEM image of La<sub>5</sub>Ni<sub>4</sub>O<sub>13-6</sub> catalyst with its SAED pattern. Right inset shows a fast Fourier transform result for the (100) direction, and indicates the observed lattice parameter for the *c*-axis.

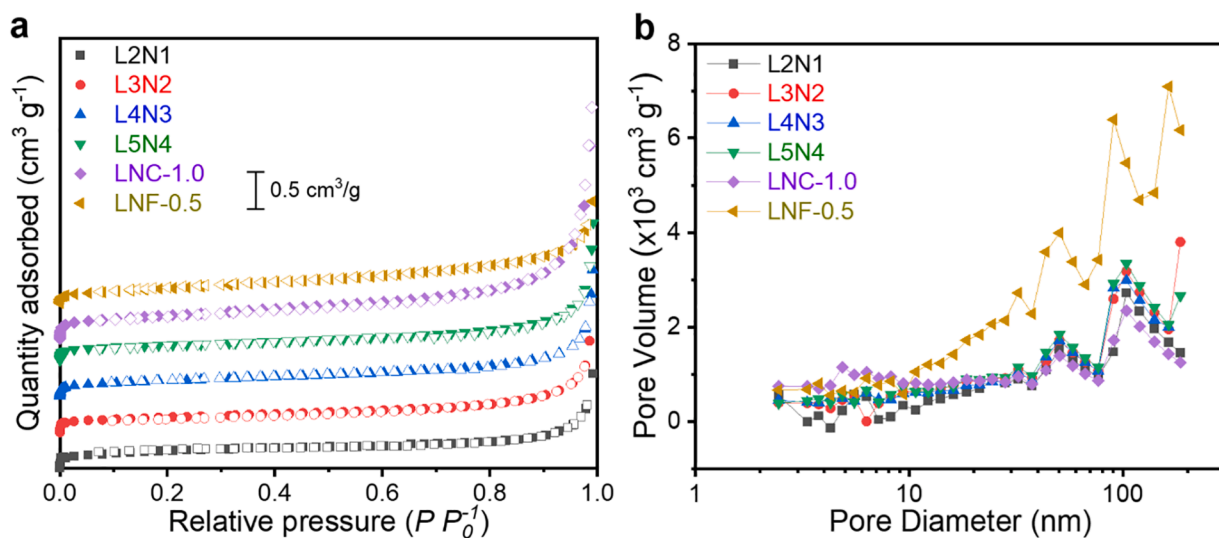


**Fig. 3.** (a) Nitrogen adsorption–desorption isotherms and (b) total pore volume and pore size of the Ruddlesden-Popper structured catalysts.

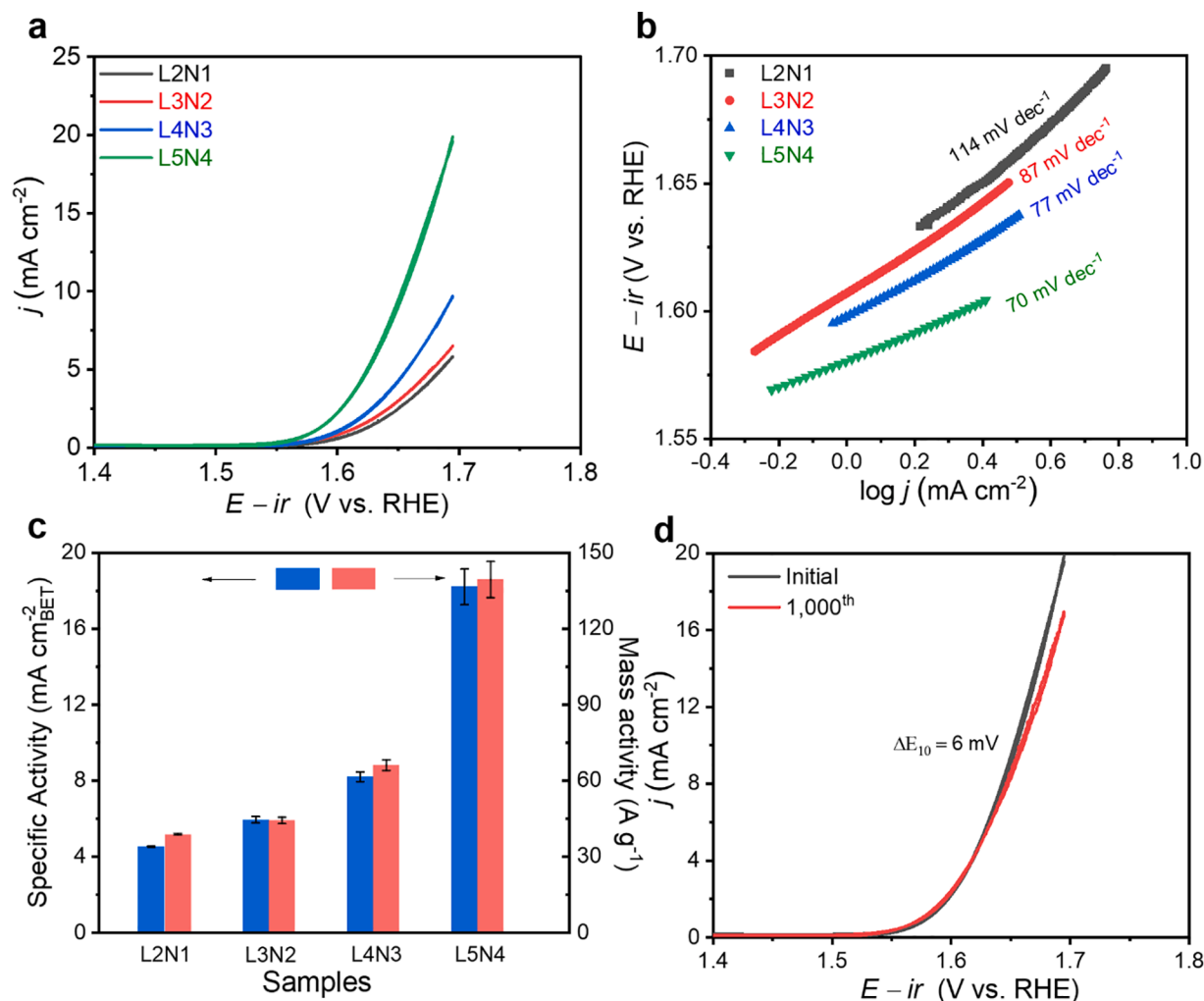


**Fig. 4.** (a) OER polarization curves, (b) corresponding OER Tafel slopes, and (c) specific and mass activity at 1.68 V (vs. RHE) of as-synthesized catalysts. (d) OER polarization curves of  $\text{La}_5\text{Ni}_4\text{O}_{13-\delta}$  (L5N4) catalysts before and after 1,000 cycles of potential sweep (1.25–1.65 V).

**Table 3**

Detailed data on electrocatalytic activities of  $\text{La}_{n+1}\text{Ni}_n\text{O}_{3n+1}$  ( $n = 1, 2, 3,$  and  $4$ ),  $\text{La}_5\text{Ni}_3\text{FeO}_{13-\delta}$ , and  $\text{La}_5\text{Ni}_3\text{CoO}_{13-\delta}$  with noble metal catalysts (Pt/C and Ir/C).

Catalyst	OER Tafel slope (mV·dec <sup>-1</sup> )	Current density@ 1.68 V(mA·cm <sup>-2</sup> )	Mass activity@ 1.68 V(A·g <sup>-1</sup> )	Specific activity@ 1.68 (mA·cm <sup>-2</sup> <sub>BET</sub> )	ORR Tafel slope (mV·dec <sup>-1</sup> )	Current density@ 0.7 V(mA·cm <sup>-2</sup> )	Mass activity@ 0.7 V(A·g <sup>-1</sup> )	Specific activity@ 0.7 V (mA·cm <sup>-2</sup> <sub>BET</sub> )
$\text{La}_2\text{NiO}_{4+\delta}$	114	4.53	38.4	4.55	167	-0.151	-1.28	-0.153
$\text{La}_3\text{Ni}_2\text{O}_{7-\delta}$	87	5.17	43.8	5.95	136	-0.407	-3.41	-0.473
$\text{La}_4\text{Ni}_3\text{O}_{10-\delta}$	77	7.75	65.4	8.18	93	-0.726	-6.17	-0.772
$\text{La}_5\text{Ni}_4\text{O}_{13-\delta}$	70	16.4	139	18.2	90	-1.19	-10.1	-1.32
$\text{La}_5\text{Ni}_3\text{CoO}_{13-\delta}$	35	55.5	470	55.7	76	-1.30	-11.0	-1.30
$\text{La}_5\text{Ni}_3\text{FeO}_{13-\delta}$	89	10.2	86.6	8.66	122	-0.686	-5.82	-0.582
Ir/C	43	28.2	203	0.289				
Pt/C					50	-4.98	-35.8	-0.0397

### 3.3. Electrochemical activity of $\text{La}_5\text{Ni}_{4-x}\text{M}_x\text{O}_{13-\delta}$ ( $M = \text{Fe}$ and $\text{Co}$ ) catalysts

The Ni-site transition metal ( $M = \text{Fe}, \text{Co}$ )-doped  $\text{La}_5\text{Ni}_{4-x}\text{M}_x\text{O}_{13-\delta}$  ( $x = 0.5, 1.0, 1.5,$  and  $2.0$ ) Ruddlesden-Popper system is of interest due to the possible improvements catalytic activity it can provide for the OER and ORR. The crystal structure of  $\text{La}_5\text{Ni}_{4-x}\text{Fe}_x\text{O}_{13-\delta}$  (LNF- $x$ ) and  $\text{La}_5\text{Ni}_{4-x}\text{Co}_x\text{O}_{13-\delta}$  (LNC- $x$ ) were studied by XRD as shown in Fig. 1c and 1d. The major phases of all samples are identified as Ruddlesden-Popper

$\text{K}_2\text{NiF}_4$  crystal structure in the XRD pattern with a minor phase that is likely indexed to NiO at high doping concentrations ( $x = 1.5, 2.0$ ) of Fe, this indicates that the Co and Fe doping did not change the crystal structure of L5N4. However, as shown in Fig. 1c and 1d, with the increase of Fe-doping content, the peak of the LNF- $x$  (220) lattice plane exhibits a slight shift to a lower angle compared to that of pure L5N4. On the other hand, the increase of the Co-doping content in the LNC- $x$  catalysts tends to cause a shift toward a higher angle. Peak shifts in the XRD patterns of the catalysts are governed by the relative ionic

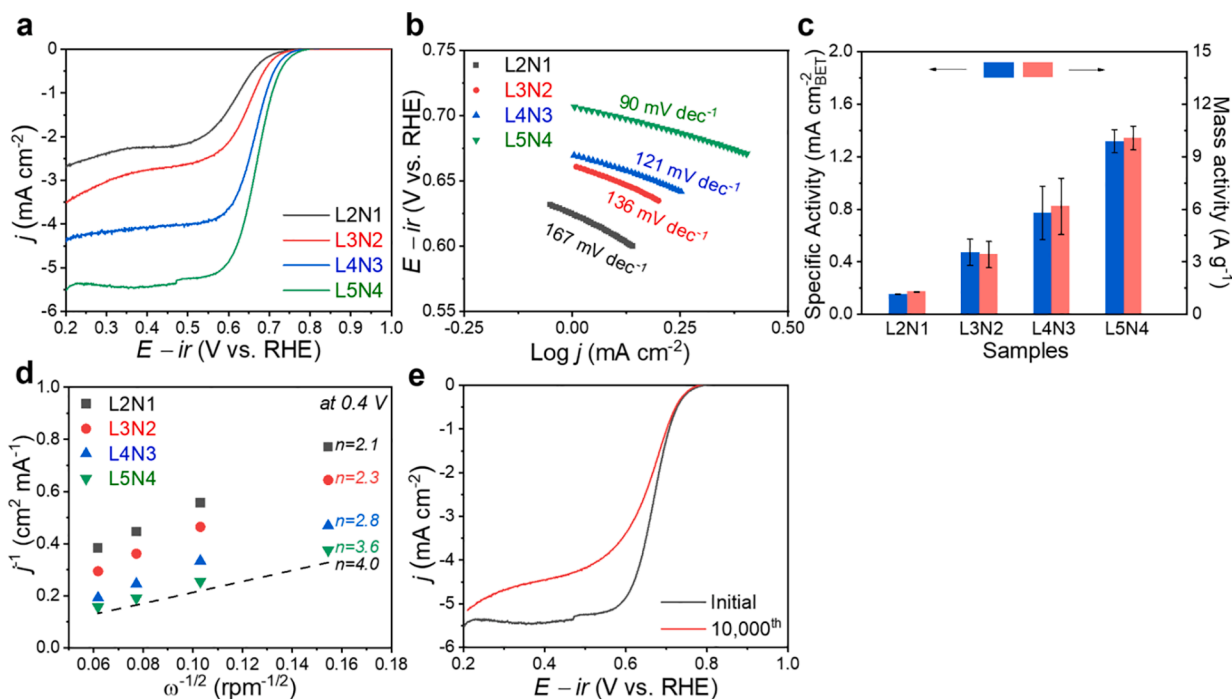


**Fig. 5.** (a) ORR polarization curves, (b) corresponding ORR Tafel slopes, (c) specific and mass activity at 0.7 V (vs. RHE), (d) electron transfer numbers from Koutecky-Levich plots of as-synthesized catalysts (at 0.4 V/RHE). (e) ORR polarization curves of  $\text{La}_5\text{Ni}_4\text{O}_{13.5}$  (L5N4) catalysts before and after 10,000 cycles of potential sweep (0.6–1.1 V).

radius ratio of the Ni and dopants for the given oxidation state ( $0.69 \text{ \AA}$  for  $\text{Ni}^{2+}$  and  $0.56 \text{ \AA}$  for  $\text{Ni}^{3+}$ ). These additional defect sites cause more exposed active sites after the modification of the electronic characteristics, this enhances the electrocatalysis for OER and ORR [43]. The electronic structure and elemental states of  $\text{La}_5\text{Ni}_{4-x}\text{M}_x\text{O}_{13.5}$  are further discussed in the next section. Size and elemental distributions of the Co and Fe-doped  $\text{La}_5\text{Ni}_{4-x}\text{M}_x\text{O}_{13.5}$  ( $\text{M} = \text{Co}, \text{Fe}$ , and  $x = 0.5, 1.0, 1.5$ , and  $2.0$ ) Ruddlesden-Popper catalysts were investigated by FESEM. The  $\text{La}_5\text{Ni}_3\text{Co}_1\text{O}_{13.5}$  (LNC-1.0) and  $\text{La}_5\text{Ni}_{2.5}\text{Fe}_{0.5}\text{O}_{13.5}$  (LNF-0.5) catalysts also exhibit severely agglomerated flake-shape morphologies that are 100–300 nm in size after synthesis by the glycine-nitrate combustion process, the constituent elements (La, Ni, Co, or Fe) were homogeneously distributed without any noticeable elemental segregation (Fig. 2e and 2f). In addition, LNC-1.0 and LNF-0.5 catalysts exhibit similar BET surface areas of 0.85 and  $1.22 \text{ m}^2\cdot\text{g}^{-1}$ , respectively, to that of L5N4 (Table 2).

The electrocatalytic OER performance of the as-prepared  $\text{La}_5\text{Ni}_{4-x}\text{Fe}_x\text{O}_{13.5}$  and  $\text{La}_5\text{Ni}_{4-x}\text{Co}_x\text{O}_{13.5}$  were evaluated in an  $\text{O}_2$ -saturated 0.1 M KOH solution with a scan rate of  $5 \text{ mV}\cdot\text{s}^{-1}$ . Due to its status as the gold standard catalyst, the Ir/C catalyst (20 wt% Ir loading, Premetek) was also tested under the same conditions. As shown in Fig. 6a and S3, LNC-1.0 exhibited the lowest overpotential of 370 mV for OER among all the samples tested and is even superior to that of Ir/C (388 mV). The overpotential at  $10 \text{ mA}\cdot\text{cm}^{-2}$ , used as an evaluation standard for solar fuel-synthesis systems, was 1.60 V for LNC-1.0 (cf. 1.65 V for Ir/C). The Tafel slopes of LNF-1.0, LNC-1.0, and Ir/C from the OER polarization curves were 89, and 35, and  $43 \text{ mV}\cdot\text{dec}^{-1}$  (cf.  $70 \text{ mV}\cdot\text{dec}^{-1}$  for L5N4), respectively, indicating exceptional OER kinetics for LNC-1.0 (Fig. 6b). Furthermore, the LNC-1.0 electrocatalyst showed much better long-term OER stability compared to Ir/C, as shown by Fig. 6c. The potential difference of LNC-1.0 at  $10 \text{ mA}\cdot\text{cm}^{-2}$  increased by 14 mV (cf., 78 mV for Ir/C) after 1,000 cycles, demonstrating the high stability of the L5N4 electrocatalyst in OER conditions. More importantly, after an extensive comparison of activities of other oxide catalysts it was found that LNC-1.0 is the best-performing oxygen electrocatalyst for OER in alkaline media ever tested (Fig. 6d and Table S1).

LSV measurements were also taken to investigate the ORR activity of the catalysts in an  $\text{O}_2$ -saturated 0.1 M KOH solution with a 1600 rpm rotating disk and a scan rate of  $5 \text{ mV}\cdot\text{s}^{-1}$  (Fig. 6e and S3c). Additionally, the Pt/C catalyst (20 wt% Pt loading, HISPEC 3000) as the gold standard catalyst for this reaction was tested under the same conditions. The ORR activity of the L5N4 was significantly improved by the doping of Co and Fe in the Ni-site of the Ruddlesden-Popper structure. In particular, the LNC-1.0 catalysts showed prominent ORR activity compared to other catalysts. Furthermore, LNC-1.0 showed a lower Tafel slope (with  $-76 \text{ mV}\cdot\text{dec}^{-1}$ ) than L5N4 ( $-90 \text{ mV}\cdot\text{dec}^{-1}$ ) and LNF-1.0 ( $-122 \text{ mV}\cdot\text{dec}^{-1}$ ) in corresponding Tafel plots (Fig. 6f and S3d), this reveals the favorable kinetics of LNC-1.0 toward ORR. As shown in Fig. 6g, LNC-1.0 exhibits a decline in ORR activity of 75 mV at  $-3 \text{ mA}\cdot\text{cm}^{-2}$ , this is comparable to the Pt/C catalyst (55 mV at  $-3 \text{ mA}\cdot\text{cm}^{-2}$ ). Moreover, the onset and half-wave potentials obtained from the LSV curves of LNC-1.0 were 0.774 and 0.668 V, respectively, these are much lower than those of Pt/C (0.980 and 0.856 V) (Table 3). Thus, further improvements in ORR activity are necessary for the successful application of this material in a bifunctional oxygen electrode, this can be achieved through the size reduction of Ruddlesden Popper particles or hybridization with electrochemically conductive graphene materials to increase the electrical conductivity of the catalyst [44,45].

To evaluate the oxygen electrode activities of the Ruddlesden-Popper structured catalysts, the potential difference ( $\Delta E$ ) between OER (at  $10 \text{ mA}\cdot\text{cm}^{-2}$ ) and ORR potentials (at  $-3 \text{ mA}\cdot\text{cm}^{-2}$ ) were calculated quantitatively, as shown in Fig. 6h and S4 [46]. A small  $\Delta E$  specifies high bifunctional oxygen electrode activity, LNC-1.0 exhibited a reasonable  $\Delta E$  value of 0.932, this is comparable to state-of-the-art oxygen catalysts (Table S2) [47–51]. As mentioned earlier, improvements in the catalytic activity of LNC-1.0 during ORR through various possible approaches will contribute to accomplishing excellent bifunctional oxygen electrode activity.

### 3.4. Mechanistic study of highly active LNC-1.0 catalysts

The outstanding electrocatalytic performances of LNC-1.0 for oxygen

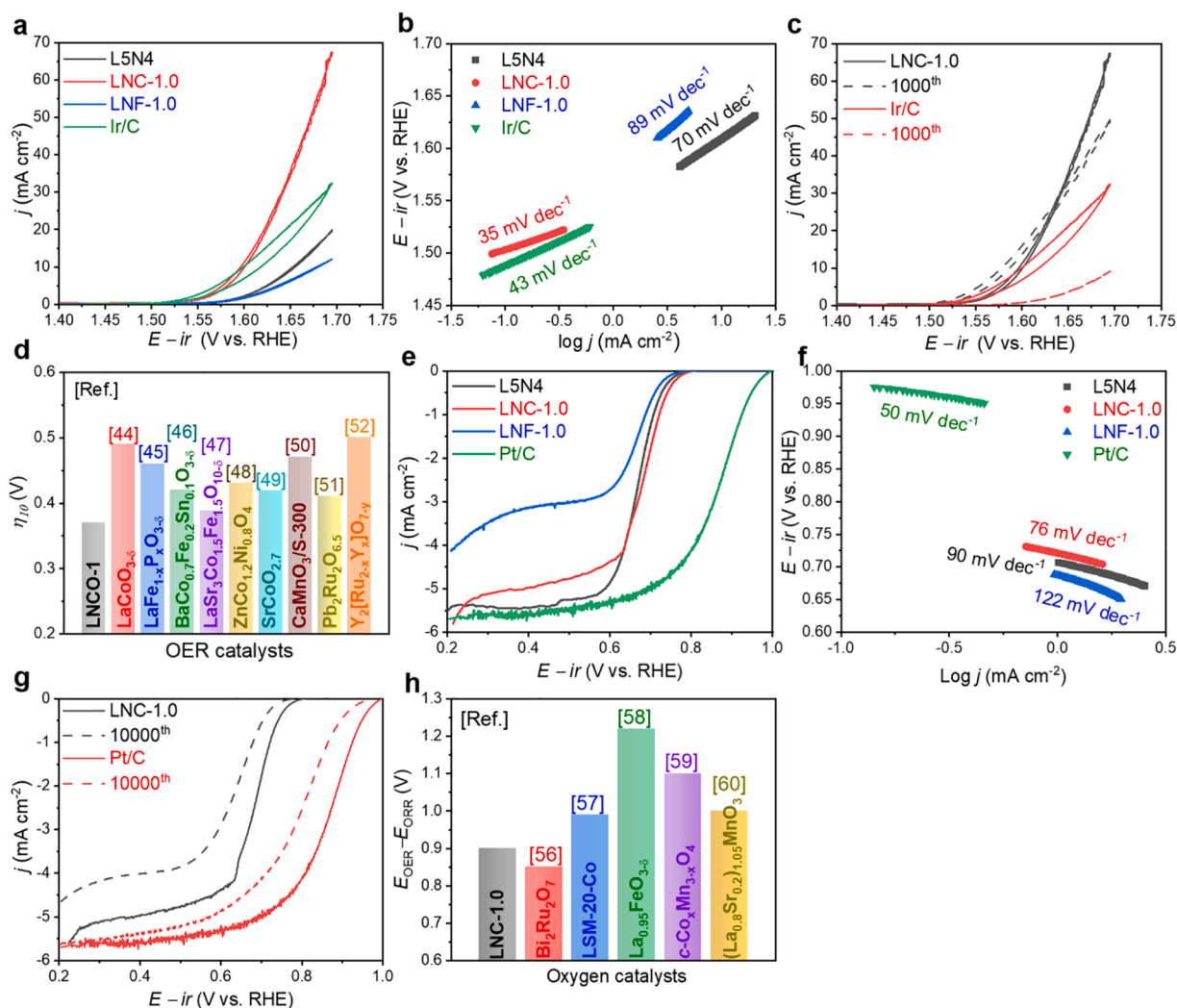


**Fig. 6.** (a) OER polarization curves and (b) corresponding OER Tafel plots of L5N4, LNC-1.0, LNF-1.0, and Ir/C catalysts. (c) OER polarization curves of LNC-1.0 and Ir/C catalysts before and after 1,000 cycles of potential sweep (1.25–1.65 V). (d) Comparison of overpotential ( $\eta_{10}$ )  $\text{mA}\cdot\text{cm}^{-2}$  for LNC-1.0 and previously reported results for other metal oxide catalysts. (e) ORR polarization curves, and (f) corresponding ORR Tafel slopes L5N4, LNC-1.0, LNF-1.0, and Ir/C catalysts. (g) ORR polarization curves of LNC-1.0 and Pt/C catalysts before and after 10,000 cycles of potential sweep (0.6–1.1 V). (h) Comparison of oxygen electrode activity ( $\Delta E$ ) for LNC-1.0 and previous reported results for other oxygen catalysts.

electrode reactions could be intrinsically dependent on its electronic configuration. To clarify the fundamental origin of the excellent OER performances of LNC-1.0, XPS was performed to investigate the surface chemical states of the catalysts (Figs. 7 and S5). Fig. 7a shows the Ni 2p core level XPS spectra of the  $\text{La}_{n+1}\text{Ni}_n\text{O}_{3n+1}$  family of catalysts, here, the main chemical states of Ni are +2 and +3. The peaks at  $\sim 854.5$  and  $\sim 851.5$  eV are considered to be from  $\text{Ni}^{2+}$  ( $2p_{1/2}$ ) and  $\text{Ni}^{2+}$  ( $2p_{3/2}$ ), respectively, while the peaks at  $\sim 864.1$  and  $\sim 849.9$  eV can be assigned to  $\text{Ni}^{3+}$  ( $2p_{1/2}$ ) and  $\text{Ni}^{3+}$  ( $2p_{3/2}$ ) [52]. Interestingly, the ratio of  $\text{Ni}^{3+}/\text{Ni}^{2+}$  increased with increasing  $n$  (the number of perovskite layers) of the Ruddlesden-Popper structure. The relative content of the various oxidation states of Ni ions was estimated from the integrated area ratios of the sub-peaks, these are listed in Table 4. The ratio of  $\text{Ni}^{3+}/\text{Ni}^{2+}$  as calculated were 0.52:1, 0.56:1, 0.69:1, 0.82:1 for L2N1, L3N2, L4N3, and L5N4, respectively. Hence, the calculated average valence of the Ni ions was determined to be 2.0, 2.50, 2.67, and 2.75 for L2N1, L3N2, L4N3, and L5N4, respectively. This is because the multivalent Ni ions can be compensated by converting lower valence  $\text{Ni}^{+2}$  to higher valence  $\text{Ni}^{+3}$  by increasing the number of oxygen vacancies in the perovskite layer in order to fulfill the electrical neutrality condition [53].

Additionally, according to previous theoretical and experimental studies, the metal–oxygen covalency increases with the increased metal

valence [54,55]. Decisively, a recent lattice-oxygen oxidation mechanism (LOM) for OER could lead to much enhanced OER activity, this mechanism bypasses the inherent thermodynamic limitation in the conventional adsorbate evolution mechanism (AEM) via a sequence of concerted proton–electron transfers on the transition metal (M)-ion centers [56,57]. This LOM for OER is promoted by the high covalency of the M–O bond, this allows the allocation of the electroactive sites from  $\text{M}^{2+}$  to  $\text{O}^{2-}$  with the formation of a ligand hole [58]. Furthermore, transition metal (Co, Fe) doping can promote the OER activity for L5N4 oxides via the LOM pathway with a synergistic effect coming from the dopant and parent cation in the Ruddlesden-Popper structure. That is, great M–O covalency caused by high  $\text{Co}^{2+,3+}$  (or  $\text{Fe}^{2+,3+}$ )/ $\text{Ni}^{2+,3+}$  content in  $\text{La}_{5-4x}\text{M}_x\text{O}_{13-8}$  results in activating surface lattice oxygen to participate in the OER, this is likely the origin of the high intrinsic activity of the Ruddlesden-Popper structured materials [59–61].

The O 1s core level XPS spectra of LNO are given in Fig. 7b, these were deconvoluted into four main components: the molecular water adsorbed on the surface ( $\text{H}_2\text{O}$ ,  $\sim 533$  eV), surface adsorbed oxygen ( $\text{O}_2/\text{OH}^-$ ,  $\sim 531$  eV), highly oxidative oxygen species ( $\text{O}_2^-/\text{O}^-$ ,  $\sim 530$  eV) and lattice oxygen species ( $\text{O}^{2-}$ ,  $\sim 528.3$  eV) [62]. The relative content of highly oxidative oxygen species on the L5N4 surface (41.1%) was apparently higher than for other Ruddlesden-Popper materials. In

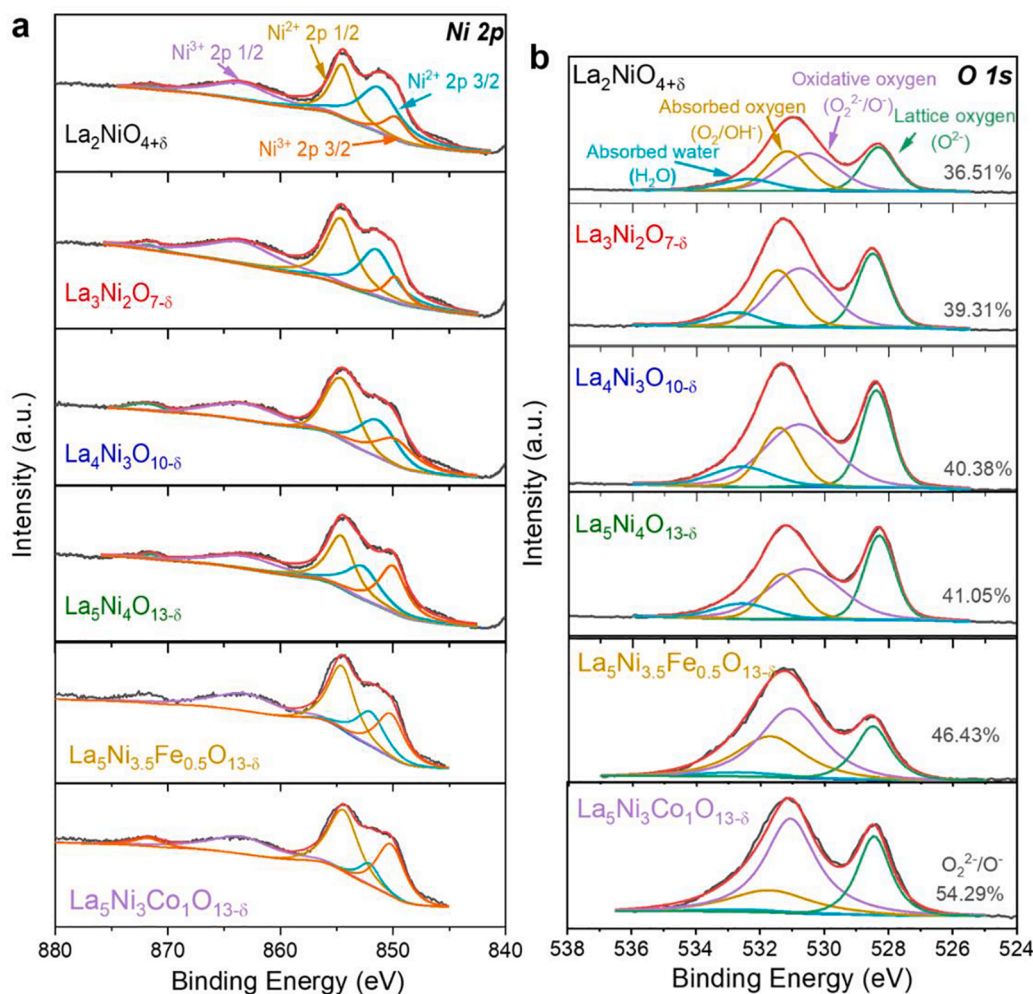


Fig. 7. XPS spectra for (a) Ni 2p and (b) O 1s of the L2N1, L3N2, L4N3, L5N4, LNF-0.5, and LNC-1.0 catalysts.

Table 4

X-ray photoelectron spectroscopy survey (showing calculated percentage ratio of oxidative oxygen and lattice oxygen, as well as peak area ratios of various oxidation states for Ni ions) for O 1s and N 2p in the  $\text{La}_{n+1}\text{Ni}_n\text{O}_{3n+1}$  ( $n = 1, 2, 3,$  and  $4$ ),  $\text{La}_5\text{Ni}_{3.5}\text{Fe}_{0.5}\text{O}_{13-\delta}$ , and  $\text{La}_5\text{Ni}_3\text{Co}_1\text{O}_{13-\delta}$  materials.

Catalysts	Oxidative oxygen ( $\text{O}_2^-/\text{O}^-$ ) (%)	Lattice oxygen ( $\text{O}^{2-}$ ) (%)	$\text{Ni}^{3+} : \text{Ni}^{2+}$ (with Co/Fe)	Average Ni-site valence
$\text{La}_2\text{NiO}_{4+\delta}$	36.51	24.80	0.52 : 1.0	+2.34 (XPS)
$\text{La}_3\text{Ni}_2\text{O}_{7-\delta}$	39.31	26.52	0.56 : 1.0	+2.36 (XPS)
$\text{La}_4\text{Ni}_3\text{O}_{10-\delta}$	40.38	27.17	0.69 : 1.0	+2.41 (XPS)
$\text{La}_5\text{Ni}_4\text{O}_{13-\delta}$	41.05	28.76	0.82 : 1.0	+2.45 (XPS)
$\text{La}_5\text{Ni}_{3.5}\text{Fe}_{0.5}\text{O}_{13-\delta}$	46.43	25.71	0.92 : 1.0	+2.53 (titration)
$\text{La}_5\text{Ni}_3\text{Co}_1\text{O}_{13-\delta}$	54.29	20.24	1.13 : 1.0	+2.56 (titration)

addition, Co- and Fe doping into L5N4 resulted in further increasing the relative content of highly oxidative oxygen species (46.4% and 54.3% for LNF-0.5 and LNC-1.0, respectively) on the catalyst surface (Table 4). This result is also evidence of a synergistic effect from the dopant and parent cation in the Ruddlesden Popper structure via the LOM pathway. Higher highly oxidative oxygen species content is correlated with the surface oxygen vacancies in the catalysts. The increasing number of perovskite layers ( $n$ ) in the Ruddlesden-Popper  $\text{La}_{n+1}\text{Ni}_n\text{O}_{3n+1}$  structure can lead to the formation of high oxygen vacancy concentrations, this is because the repeated stacking of lanthanide causes a structural

distortion of the lattice in perovskite systems, this generates the extra oxygen vacancies via structural deformation [63]. As calculated from the Ni-site oxidation state using the iodometric titration method [64], the nonstoichiometric  $\delta$  values of L2N1, L3N2, L4N3, L5N4, LNF-1.0, and LNC-1.0 were determined to be 0.08, -0.05, -0.13, -0.21, -0.45, and -0.39, respectively, they are in good agreements with previously reported results [65]. It is known that L2N1 has interstitial oxygen content which resides in the LaO layers. Hence, the negative value of  $\delta$  specifies the generation of extra oxygen vacancies with increasing  $n$  (=the number of perovskite layers) in the Ruddlesden-Popper structure, this is in agreement with the results of the XPS O 1s spectra analysis.

The high  $\text{O}_2^-/\text{O}^-$  content can lead to an improved oxygen-ion diffusion rate and electrical conductivity due to the existence of abundant surface oxygen vacancies. We measured the oxygen-ion diffusion coefficient ( $D_o$ ) of L2N1, L5N4, and LNC-1.0 and evaluated their influence on the OER activity to further support LOM as being the origin of the high intrinsic activity of LNC-1.0.  $D_o$  was determined using combined chronoamperometry and CV measurements for the insertion and extraction of oxygen-ions with an RDE (Fig. S6a) [35-37]. Current ( $i$ ) vs.  $t^{-1/2}$  was plotted in Fig. S6b to obtain the intercept with the  $t^{-1/2}$  axis (at  $i = 0$ ). The  $D_o$  value of LNC-1.0 was calculated to be  $2.134 \times 10^{-11} \text{ cm}^2 \text{ s}^{-1}$ , this is  $\sim 5.0$  and  $3.6$  times faster than that of L2N1 and L5N4, respectively, as presented in Fig. 8a. Consequently, fast  $D_o$  will activate the surface lattice-oxygen by replenishing the surface oxygen consumed during the catalytic OER process. The pH dependence of OER activity on the RHE scale also indicates LOM participation in alkaline medium reactions, this is evidence for the presence of non-concerted

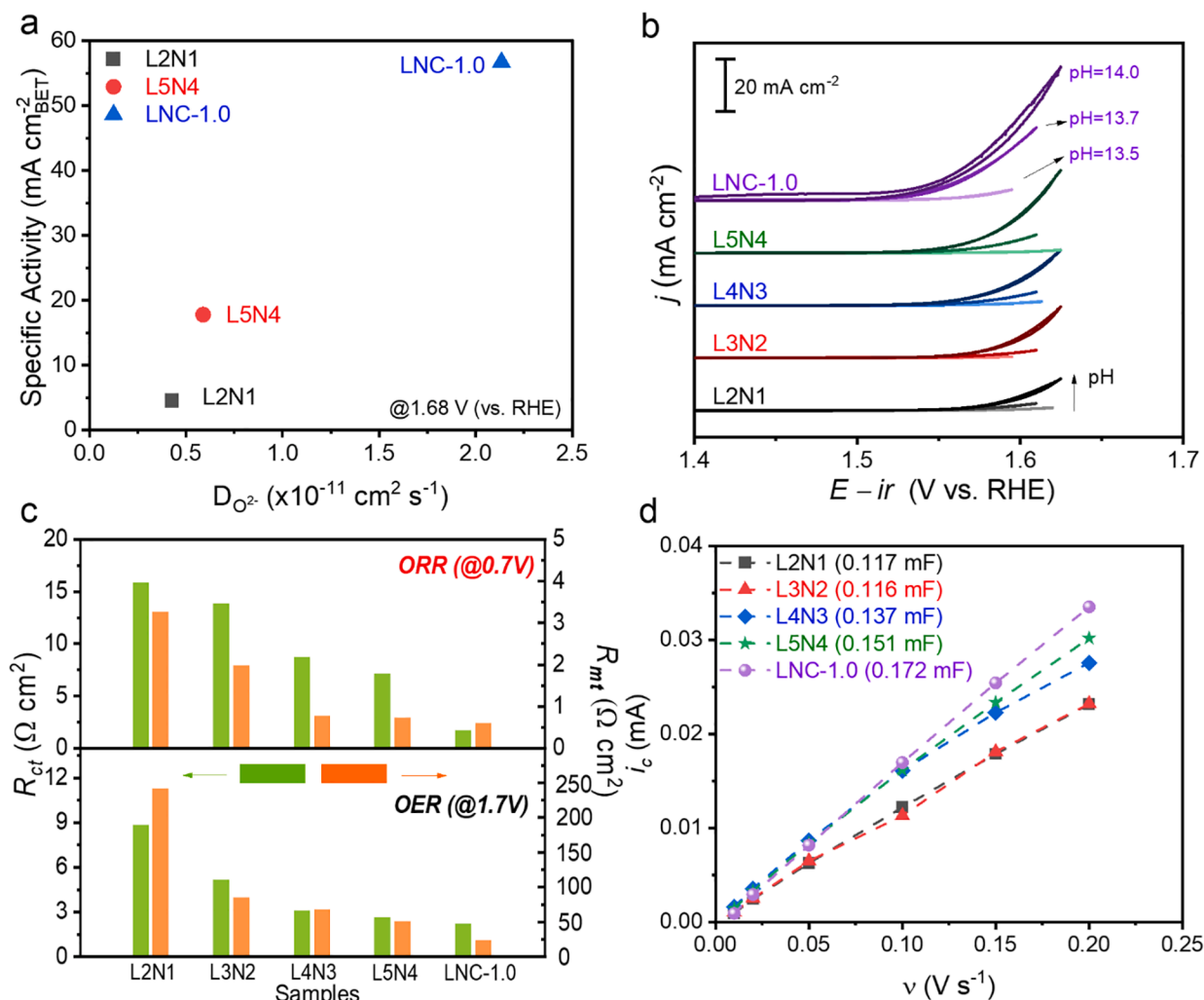


**Fig. 8.** (a) Correlation of specific activity with oxygen-ion diffusion coefficient to scrutinize the intrinsic OER activity of catalysts. (b) OER kinetic currents of catalysts in  $O_2$ -saturated KOH (0.1, 0.5, and 1 M) electrolytes under various pH. (c) Charge-transfer ( $R_{ct}$ ) and mass transfer resistances ( $R_{mt}$ ) of catalysts for OER at 1.7 V and ORR at 0.7 V from complex-plane Nyquist EIS plots. (d) Double layer charging current of catalysts calculated from CVs with different scan rate (10–200  $\text{mV} \cdot \text{s}^{-1}$ ) in non-faradaic potential range.

proton–electron transfer steps during the OER. OER currents from CV measurements were found to increase while increasing pH from 13.5 to 14.0 for the Ruddlesden-Popper structured LNO ( $n = 1-4$ ) and LNC-1.0 (seen in Fig. 8b), this in agreement with the results in previous literature concerning LOM participation in the OER [36,60,66,67].

To understand the fundamental origin of the excellent OER performances of LNC-1.0, electrochemical impedance spectroscopy (EIS) was performed in a three-electrode cell to analyze the resistance components [ohmic resistance ( $R_{ohmic}$ ) of solution electrolyte, charge-transfer resistance ( $R_{ct}$ ), and mass-transfer resistance ( $R_{mt}$ )] [67,68]. Fig. S7 shows complex-plane Nyquist plots of LNO and LNC-1.0 catalysts at 1.7 and 0.7 V (vs. RHE) for OER and ORR. The  $R_{ct}$  and  $R_{mt}$  values of the catalysts significantly decrease in the order from smallest to biggest decreases of L2N1, L3N2, L4N3, and L5N4 for both OER and ORR. This indicates the excellent intrinsic activity of high  $n$  Ruddlesden-Popper structure electrocatalysts (Fig. 8c). In addition, LNC-1.0 exhibits the lowest  $R_{ct}$  of 2.15 and  $1.65 \Omega \cdot \text{cm}^2$  among all the test samples, at 1.7 and 0.7 V (vs. RHE) for OER and ORR, respectively, this confirms the most effective conducting path for charged ionic/electronic species in oxygen electrode reactions. The electrochemically active surface area (ECSA) of the catalyst was also calculated by dividing the double layer capacitance ( $C_{dl}$ ) by specific capacitance ( $C_s \approx 0.04 \text{ mF} \cdot \text{cm}^{-2}$ ), this is a critical indicator of catalysts for catalytic activity [69,70].  $C_{dl}$  was determined by calculating the

slopes of the measured charging current ( $i_c$ ) plots as a function of  $\nu$  (Fig. 8d) that come from the CVs of various scan rates ( $\nu = 10, 20, 50, 100, 150,$  and  $200 \text{ mV} \cdot \text{s}^{-1}$ ) (Fig. S8). The ECSA of LNC-1.0 was  $4.30 \text{ cm}^2$ , which is higher than that of L2N1 ( $2.93 \text{ cm}^2$ ), L3N2 ( $2.90 \text{ cm}^2$ ), L4N3 ( $3.43 \text{ cm}^2$ ), and L5N4 ( $3.78 \text{ cm}^2$ ).

#### 4. Conclusion

We demonstrated transition metal ( $M = \text{Fe}, \text{Co}$ )-doped  $\text{La}_{n+1}\text{Ni}_n\text{-xM}_x\text{O}_{3n+1}$  ( $n = 1, 2, 3,$  and  $4$ ) with an  $n$  layered perovskite structures are highly active during OER and ORR in alkaline medium. In particular, 4 layered perovskite LNM catalysts were successfully synthesized with various dopants via GNC techniques under extremely fuel-rich conditions. The formation of high order L5N4 Ruddlesden-Popper phases was confirmed through quantitative analysis with FESEM (and HRTEM)/EDX and SAED pattern observed along the  $[100]$  zone axis of HRTEM image, this in agreement with the results obtained from the Rietveld refinement of the XRD results. The catalytic activity of LNO increased with the number of perovskite layers at room temperature in alkaline medium. Benefiting from its 4 layered perovskite structure with transition metal dopants, the  $\text{La}_5\text{Ni}_3\text{CoO}_{13.6}$  catalysts exhibited outstanding bifunctional electrocatalytic activity with low overpotential and Tafel slopes for both OER and ORR. LNC-1.0 showed superior OER activity

with extremely low overpotential (1.60 V at 10 mA·cm<sup>-2</sup>) and Tafel slope (35 mV·dec<sup>-1</sup>) that were superior to the other catalysts. Furthermore, LNC-1.0 showed excellent long-term OER and ORR durability. Increasing the number of perovskite layers (*n*) in the Ruddlesden-Popper La<sub>n+1</sub>Ni<sub>n</sub>O<sub>3n+1</sub> structure can lead to the formation of abundant surface oxygen vacancy concentrations and enriched electronic charge carriers due to the increased Ni oxidation state. Furthermore, the high O<sub>2</sub><sup>2-</sup>/O<sup>-</sup> content can lead to an improved oxygen-ion diffusion rate and superior electrical conductivity, this in turn results in the exceptional OER performances of LNC-1.0.

## Declaration of Competing Interest

The authors declare that they have no known competing financial interests or personal relationships that could have appeared to influence the work reported in this paper.

## Acknowledgments

This research was supported by the Climate Change Technology Research Program (NRF-2015M1A2A2057042), Technology Development Program to Hydrogen Energy (NRF-2019M3E6A1064020) through the National Research Foundation funded by the Ministry of Science and ICT of Korea, and Technology Innovation Program (20011633) funded by the Ministry of Trade, Industry & Energy of (MOTIE) Korea.

## Appendix A. Supplementary data

Supplementary data to this article can be found online at <https://doi.org/10.1016/j.cej.2020.128226>.

## References

- [1] W.T. Hong, K.A. Stoerzinger, Y.-L. Lee, L. Giordano, A. Grimaud, A.M. Johnson, J. Hwang, E.J. Crumlin, W. Yang, Y. Shao-Horn, Charge-transfer-energy-dependent oxygen evolution reaction mechanisms for perovskite oxides, *Energy Environ. Sci.* 10 (10) (2017) 2190–2200.
- [2] J.W.D. Ng, M. Tang, T.F. Jaramillo, A carbon-free, precious-metal-free, high-performance O<sub>2</sub> electrode for regenerative fuel cells and metal-air batteries, *Energy Environ. Sci.* 7 (6) (2014) 2017, <https://doi.org/10.1039/c3ee44059a>.
- [3] B.T. Zhao, L. Zhang, D.X. Zhen, S. Yoo, Y. Ding, D.C. Chen, Y. Chen, Q.B. Zhang, B. Doyle, X.H. Xiong, M.L. Liu, A tailored double perovskite nanofiber catalyst enables ultrafast oxygen evolution, *Nat. Commun.* 8 (2017) 14586.
- [4] J. Yang, T. Fujigaya, N. Nakashima, Decorating unoxidized-carbon nanotubes with homogeneous Ni-Co spinel nanocrystals show superior performance for oxygen evolution/reduction reactions, *Sci. Rep.* 7 (2017) 45384.
- [5] S.-W. Kim, Y. Son, K. Choi, S.-I. Kim, Y. Son, J. Park, J.H. Lee, J.-H. Jang, Highly Active Bifunctional Electrocatalysts for Oxygen Evolution and Reduction in Zn-Air Batteries, *ChemSusChem* 11 (24) (2018) 4203–4208.
- [6] S. Gadipelli, T. Zhao, S.A. Shevlin, Z. Guo, Switching effective oxygen reduction and evolution performance by controlled graphitization of a cobalt–nitrogen–carbon framework system, *Energy Environ. Sci.* 9 (5) (2016) 1661–1667.
- [7] J. Wandt, A.T.S. Freiberg, A. Ogrodnik, H.A. Gasteiger, Singlet oxygen evolution from layered transition metal oxide cathode materials and its implications for lithium-ion batteries, *Materials Today* 21 (8) (2018) 825–833.
- [8] L. Du, L.L. Luo, Z.X. Feng, M. Engelhard, X.H. Xie, B.H. Han, J.M. Sun, J.H. Zhang, G.P. Yin, C.M. Wang, Y. Wang, Y.Y. Shao, Nitrogen-doped graphitized carbon shell encapsulated NiFe nanoparticles: A highly durable oxygen evolution catalyst, *Nano Energy* 39 (2017) 245–252.
- [9] Y. Wang, J. Li, Z. Wei, Transition-metal-oxide-based catalysts for the oxygen reduction reaction, *J. Mater. Chem. A* 6 (18) (2018) 8194–8209.
- [10] Y. Xue, S. Sun, Q. Wang, Z. Dong, Z. Liu, Transition metal oxide-based oxygen reduction reaction electrocatalysts for energy conversion systems with aqueous electrolytes, *J. Mater. Chem. A* 6 (23) (2018) 10595–10626.
- [11] J.-I. Jung, M. Risch, S. Park, M.G. Kim, G. Nam, H.-Y. Jeong, Y. Shao-Horn, J. Cho, Optimizing nanoparticle perovskite for bifunctional oxygen electrocatalysis, *Energy Environ. Sci.* 9 (1) (2016) 176–183.
- [12] H. Asano, J. Hayakawa, M. Matsui, Preparation and properties of triple perovskite La<sub>3-3x</sub>Ca<sub>1+3x</sub>Mn<sub>3</sub>O<sub>10</sub> ferromagnetic thin films, *Appl. Phys. Lett.* 71 (6) (1997) 844–846.
- [13] N.-I. Kim, R.A. Afzal, S.R. Choi, S.W. Lee, D. Ahn, S. Bhattacharjee, S.-C. Lee, J. H. Kim, J.-Y. Park, Highly active and durable nitrogen doped-reduced graphene oxide/double perovskite bifunctional hybrid catalysts, *J. Mater. Chem. A* 5 (25) (2017) 13019–13031.
- [14] N.-I. Kim, Y.J. Sa, T.S. Yoo, S.R. Choi, R.A. Afzal, T. Choi, Y.-S. Seo, K.-S. Lee, J. Y. Hwang, W.S. Choi, S.H. Joo, J.-Y. Park, Oxygen-deficient triple perovskites as highly active and durable bifunctional electrocatalysts for oxygen electrode reactions, *Sci. Adv.* 4 (6) (2018) eaap9360, <https://doi.org/10.1126/sciadv.aap9360>.
- [15] J. Suntivich, K.J. May, H.A. Gasteiger, J.B. Goodenough, Y. Shao-Horn, A perovskite oxide optimized for oxygen evolution catalysis from molecular orbital principles, *Science* 334 (6061) (2011) 1383–1385.
- [16] S. Takahashi, S. Nishimoto, M. Matsuda, M. Miyake, Electrode properties of the Ruddlesden-Popper series, La<sub>n+1</sub>Ni<sub>n</sub>O<sub>3n+1</sub> (n=1, 2, and 3), as intermediate-temperature solid oxide fuel cells, *J. Am. Ceram. Soc.* 93 (2010) 2329–2333.
- [17] S. Yoo, S. Choi, J. Shin, M. Liu, G. Kim, Electrical properties, thermodynamic behavior, and defect analysis of La<sub>n+1</sub>Ni<sub>n</sub>O<sub>3n+1+δ</sub> infiltrated into YSZ scaffolds as cathodes for intermediate-temperature SOFCs, *RSC Adv.* 2 (11) (2012) 4648, <https://doi.org/10.1039/c2ra20402a>.
- [18] S. Choi, S. Yoo, J.Y. Shin, G. Kim, High performance SOFC cathode prepared by infiltration of La<sub>n+1</sub>Ni<sub>n</sub>O<sub>3n+1</sub> (n=1, 2, and 3) in porous YSZ, *J. Electrochem. Soc.* 158 (2011) B995–B999.
- [19] S.N. Ruddlesden, P. Popper, New compounds of the K<sub>2</sub>NiF<sub>4</sub> type, *Acta Cryst.* 10 (8) (1957) 538–539.
- [20] E. Boehm, J.M. Bassat, P. Dordor, F. Mauvy, J.C. Grenier, P. Stevens, Oxygen diffusion and transport properties in non-stoichiometric Ln<sub>2-x</sub>NiO<sub>4+δ</sub> oxides, *Solid State Ionics* 176 (2005) 2717–2725.
- [21] M. Matsuda, M. Hashimoto, C. Matsunaga, T.S. Suzuki, Y. Sakka, T. Uchikoshi, Electrodeposition fabrication of a-b plane oriented La<sub>2</sub>NiO<sub>4</sub> cathode onto electrolyte in strong magnetic field for low-temperature operating solid oxide fuel cell, *Journal of the European Ceramic Society* 36 (16) (2016) 4077–4082.
- [22] D. Cetin, S. Poizeau, J. Pietras, S. Gopalan, Decomposition of La<sub>2</sub>NiO<sub>4</sub> in Sm<sub>0.2</sub>Ce<sub>0.8</sub>O<sub>2</sub>-La<sub>2</sub>NiO<sub>4</sub> composites for solid oxide fuel cell applications, *Solid State Ionics* 300 (2017) 91–96.
- [23] P. Li, B. Yu, J. Li, X. Yao, Y. Zhao, Y. Li, A single layer solid oxide fuel cell composed of La<sub>2</sub>NiO<sub>4</sub> and doped ceria-carbonate with H<sub>2</sub> and methanol as fuels, *International Journal of Hydrogen Energy* 41 (21) (2016) 9059–9065.
- [24] J. Yu, J. Sunarso, Y. Zhu, X. Xu, R. Ran, W. Zhou, Z. Shao, Activity and stability of Ruddlesden-Popper-Type La<sub>n+1</sub>Ni<sub>n</sub>O<sub>3n+1</sub> (n=1, 2, 3, and ∞) electrocatalysts for oxygen reduction and evolution reactions in alkaline media, *Chem. Eur. J.* 22 (8) (2016) 2719–2727.
- [25] X. Ma, B. Wang, E. Xhafa, K. Sun, E. Nikolla, Synthesis of shape-controlled La<sub>2</sub>NiO<sub>4+δ</sub> nanostructures and their anisotropic properties for oxygen diffusion, *Chem. Commun.* 51 (1) (2015) 137–140.
- [26] M.D. Carvalho, F.M.A. Costa, I.D.S. Pereira, A. Wattiaux, J.M. Bassat, J.C. Grenier, M. Pouchard, New preparation method of La<sub>n+1</sub>Ni<sub>n</sub>O<sub>3n+1+δ</sub> (n=2, 3), *J. Mater. Chem.* 7 (1997) 2107–2111.
- [27] R.D. Purohit, B.P. Sharma, K.T. Pillai, A.K. Tyagi, Ultrafine ceria powders via glycine-nitrate combustion, *Materials Research Bulletin* 36 (15) (2001) 2711–2721.
- [28] A. Varma, A.S. Mukasyan, A.S. Rogachev, K.V. Manukyan, Solution Combustion Synthesis of Nanoscale Materials, *Chem. Rev.* 116 (23) (2016) 14493–14586.
- [29] A. Wain-Martin, A. Morán-Ruiz, K. Vidal, A. Larranaga, M.A. Laguna-Bercero, M. I. Arriortua, Scalable synthetic method for SOFC compounds, *Solid State Ionics* 313 (2017) 52–57.
- [30] Z. Ming, Z. Lu, Y. Chunzhen, C. Yao, S. Zhongrong, C. Bo, All-nanosheet OER/ORR bifunctional electrocatalyst for both aprotic and aqueous Li-O<sub>2</sub> batteries, *Nanoscale* 11 (2019) 2855–2862.
- [31] Y. Jiang, Y.P. Deng, J. Fu, D.U. Lee, R.L. Liang, Z.P. Cano, Y.S. Liu, Z.Y. Bai, S. Hwang, L. Yang, D. Su, W.G. Chu, Z.W. Chen, Interpenetrating triphase cobalt-based nanocomposites as efficient bifunctional oxygen electrocatalysts for long-lasting rechargeable Zn-air batteries, *Adv. Energy Mater.* 8 (2018) 1702900.
- [32] Y.X. Lin, L. Yang, Y.K. Zhang, H.L. Jiang, Z.J. Xiao, C.Q. Wu, G.B. Zhang, J. Jiang, L. Song, Defective carbon-CoP nanoparticles hybrids with interfacial charges polarization for efficient bifunctional oxygen electrocatalysis, *Adv. Energy Mater.* 8 (2018) 1703623.
- [33] S. Yagi, I. Yamada, H. Tsukasaki, A. Seno, M. Murakami, H. Fujii, H. Chen, N. Umezawa, H. Abe, N. Nishiyama, S. Mori, Covalency-reinforced oxygen evolution reaction catalyst, *Nat. Commun.* 6 (2015) 8249.
- [34] A. Grimaud, O. Diaz-Morales, B. Han, W.T. Hong, Y.-L. Lee, L. Giordano, K. A. Stoerzinger, M.T.M. Koper, Y. Shao-Horn, Activating lattice oxygen redox reactions in metal oxides to catalyze oxygen evolution, *Nature Chem* 9 (5) (2017) 457–465.
- [35] J.T. Mefford, X. Rong, A.M. Abakumov, W.G. Hardin, S. Dai, A.M. Kolpak, K. P. Johnston, K.J. Stevenson, Water electrolysis on La<sub>1-x</sub>Sr<sub>x</sub>CoO<sub>3-δ</sub> perovskite electrocatalysts, *Nat. Commun.* 7 (2016) 11053.
- [36] Y. Pan, X. Xu, Y. Zhong, L. Ge, Y. Chen, J.-P.-M. Veder, D. Guan, R. O'Hayre, M. Li, G. Wang, H. Wang, W. Zhou, Z. Shao, Direct evidence of boosted oxygen evolution over perovskite by enhanced lattice oxygen participation, *Nat. Commun.* 11 (2020) 2002.
- [37] F.R. Van Buren, G.H.J. Broers, A.J. Bouman, C. Boesveld, The electrochemical determination of oxygen ion diffusion coefficients in La<sub>0.50</sub>Sr<sub>0.50</sub>CoO<sub>3-y</sub>, *Journal of Electroanalytical Chemistry and Interfacial Electrochemistry* 88 (3) (1978) 353–361.
- [38] M. Jungbauer, S. Huhn, R. Egoavil, H. Tan, J. Verbeeck, G. Van Tendeloo, V. Moshnyaga, Atomic layer epitaxy of Ruddlesden-Popper SrO(SrTiO<sub>3</sub>)<sub>n</sub> films by means of metalorganic aerosol deposition, *Appl. Phys. Lett.* 105 (2014), 251603.

- [39] R.K. Sharma, M. Burriel, E. Djurado,  $\text{La}_4\text{Ni}_3\text{O}_{10.5}$  as an efficient solid oxide fuel cell cathode: electrochemical properties versus microstructure, *J. Mater. Chem. A* 3 (2015) 23833–23843.
- [40] N. Gauquelin, T.E. Weirich, M. Ceretti, W. Paulus, M. Schroeder, Long-term structural surface modifications of mixed conducting  $\text{La}_2\text{NiO}_{4+\delta}$  at high temperatures, *Monatsh Chem* 140 (9) (2009) 1095–1102.
- [41] J. Kibsgaard, I.B. Chorkendorff, Considerations for the scaling-up of water splitting catalysts, *Nat Energy* 4 (6) (2019) 430–433.
- [42] S. Liu, I.S. Amiinu, X. Liu, J. Zhang, M. Bao, T. Meng, S. Mu, Carbon nanotubes intercalated Co/N-doped porous carbon nanosheets as efficient electrocatalyst for oxygen reduction reaction and zinc–air batteries, *Chemical Engineering Journal* 342 (2018) 163–170.
- [43] Y. Zhu, X.i. Liu, S. Jin, H. Chen, W. Lee, M. Liu, Y. Chen, Anionic defect engineering of transition metal oxides for oxygen reduction and evolution reactions, *J. Mater. Chem. A* 7 (11) (2019) 5875–5897.
- [44] S.M. Zhou, X.B. Miao, X. Zhao, C. Ma, Y.H. Qiu, Z.P. Hu, J.Y. Zhao, L. Shi, J. Zeng, Engineering electrocatalytic activity in nanosized perovskite cobaltite through surface spin-state transition, *Nat. Commun.* 7 (2016) 11510.
- [45] S. Li, X. Meng, Q. Yi, J.A. Alonso, M.T. Fernández-Díaz, C. Sun, Z.L. Wang, Structural and electrochemical properties of  $\text{LiMn}_{0.6}\text{Fe}_{0.4}\text{PO}_4$  as a cathode material for flexible lithium-ion batteries and self-charging power pack, *Nano Energy* 52 (2018) 510–516.
- [46] X.M. Xu, C. Su, W. Zhou, Y.L. Zhu, Y.B. Chen, Z.P. Shao, Co-doping strategy for developing perovskite oxides as highly efficient electrocatalysts for oxygen evolution reaction, *Adv. Sci.* 3 (2016) 1500187.
- [47] S. Liu, H. Luo, Y. Li, Q. Liu, J.-L. Luo, Structure-engineered electrocatalyst enables highly active and stable oxygen evolution reaction over layered perovskite  $\text{LaSr}_3\text{Co}_{1.5}\text{Fe}_{1.5}\text{O}_{10-\delta}$ , *Nano Energy* 40 (2017) 115–121.
- [48] Y. Duan, S.N. Sun, Y.M. Sun, S.B. Xi, X. Chi, Q.H. Zhang, X. Ren, J.X. Wang, S.J. H. Ong, Y.H. Du, L. Gu, A. Grimaud, Z.C.J. Xu, Mastering surface reconstruction of metastable spinel oxides for better water oxidation, *Adv. Mater.* 31 (2019) 1807898.
- [49] J.G. Lee, J. Hwang, H.J. Hwang, O.S. Jeon, J. Jang, O. Kwon, Y. Lee, B. Han, Y.-G. Shul, A New Family of Perovskite Catalysts for Oxygen-Evolution Reaction in Alkaline Media:  $\text{BaNiO}_3$  and  $\text{BaNi}_{0.83}\text{O}_{2.5}$ , *J. Am. Chem. Soc.* 138 (10) (2016) 3541–3547.
- [50] I. Yamada, M. Murakami, N. Hayashi, S. Mori, Inverse charge transfer in the quadruple perovskite  $\text{CaCu}_3\text{Fe}_4\text{O}_{12}$ , *Inorg. Chem.* 55 (4) (2016) 1715–1719.
- [51] J. Park, M. Risch, G. Nam, M. Park, T.J. Shin, S. Park, M.G. Kim, Y. Shao-Horn, J. Cho, Single crystalline pyrochlore nanoparticles with metallic conduction as efficient bi-functional oxygen electrocatalysts for Zn–air batteries, *Energy Environ. Sci.* 10 (1) (2017) 129–136.
- [52] J. Park, M. Park, G. Nam, M.G. Kim, J. Cho, Unveiling the catalytic origin of nanocrystalline yttrium ruthenate pyrochlore as a bifunctional electrocatalyst for Zn–air batteries, *Nano Lett.* 17 (6) (2017) 3974–3981.
- [53] Y. Li, Z.S. Wu, P. Lu, X. Wang, W. Liu, J. Ma, W. Ren, Z. Jiang, X. Bao, High-Valence Nickel Single-Atom Catalysts Coordinated to Oxygen Sites for Extraordinarily Activating Oxygen Evolution Reaction, *Adv. Sci.* 7 (2020) 1903089–1903097.
- [54] N.-I. Kim, S.-H. Cho, S.H. Park, Y.J. Lee, R.A. Afzal, J. Yoo, Y.-S. Seo, Y.J. Lee, J.-Y. Park, B-site doping effects of  $\text{NdBa}_{0.75}\text{Ca}_{0.25}\text{Co}_2\text{O}_{5+\delta}$  double perovskite catalysts for oxygen evolution and reduction reactions, *J. Mater. Chem. A* 6 (36) (2018) 17807–17818.
- [55] C. Su, T. Yang, W. Zhou, W. Wang, X. Xu, Z. Shao, Pt/C–LiCoO<sub>2</sub> composites with ultralow Pt loadings as synergistic bifunctional electrocatalysts for oxygen reduction and evolution reactions, *J. Mater. Chem. A* 4 (12) (2016) 4516–4524.
- [56] M. Kim, H. Ju, J. Kim, Single crystalline  $\text{Bi}_2\text{Ru}_2\text{O}_7$  pyrochlore oxide nanoparticles as efficient bifunctional oxygen electrocatalyst for hybrid Na-air batteries, *Chem. Eng. J.* 358 (2019) 11–19.
- [57] A. Seong, J. Kim, O. Kwon, H.Y. Jeong, R.J. Gorte, J.M. Vohs, G. Kim, Self-reconstructed interlayer derived by in-situ Mn diffusion from  $\text{La}_{0.5}\text{Sr}_{0.5}\text{MnO}_3$  via atomic layer deposition for an efficient bi-functional electrocatalyst, *Nano Energy* 71 (2020), 104564.
- [58] Y. Zhu, W. Zhou, J. Yu, Y. Chen, M. Liu, Z. Shao, Enhancing electrocatalytic activity of perovskite oxides by tuning cation deficiency for oxygen reduction and evolution reactions, *Chem. Mater.* 28 (6) (2016) 1691–1697.
- [59] C. Li, X.P. Han, F.Y. Cheng, Y.X. Hu, C.C. Chen, J. Chen, Phase and composition controllable synthesis of cobalt manganese spinel nanoparticles towards efficient oxygen electrocatalysis, *Nat. Commun.* 6 (2015) 7345.
- [60] W. Xu, N. Apodaca, H. Wang, L. Yan, G. Chen, M. Zhou, D. Ding, P. Choudhury, H. Luo, A-site excessive ( $\text{La}_{0.8}\text{Sr}_{0.2}{}_{1+x}\text{MnO}_3$ ) perovskite oxides for bifunctional oxygen catalyst in alkaline media, *ACS Catal.* 9 (6) (2019) 5074–5083.
- [61] H.M. Sun, Y.X. Ye, Z.F. Tian, S.L. Wu, J. Liu, C.H. Liang,  $\text{Ni}^{3+}$  doped cobalt–nickel layered double hydroxides as high-performance electrode materials for supercapacitors, *RSC Adv.* 7 (77) (2017) 49010–49014.
- [62] L. Wang, K.A. Stoerzinger, L. Chang, J.L. Zhao, Y.Y. Li, C.S. Tang, X.M. Yin, M. E. Bowden, Z.Z. Yang, H.Z. Guo, L. You, R. Guo, J. Wang, K. Ibrahim, J.S. Chen, A. Ruyadi, J.L. Wang, S.A. Chambers, Y.G. Du, Tuning bifunctional oxygen electrocatalysts by changing the A-Site rare-earth element in perovskite nickelates, *Adv. Funct. Mater.* 28 (2018) 1803712.
- [63] R. Nakajima, J. Stohr, Y.U. Idzherda, Electron-yield saturation effects in L-edge x-ray magnetic circular dichroism spectra of Fe Co, and Ni, *Phys. Rev. B* 59 (1999) 6421–6429.
- [64] D.Q. Guan, J. Zhou, Z.W. Hu, W. Zhou, X.M. Xu, Y.J. Zhong, B. Liu, Y.H. Chen, M. G. Xu, H.J. Lin, C.T. Chen, J.Q. Wang, Z.P. Shao, Searching general sufficient-and-necessary conditions for ultrafast hydrogen-evolving electrocatalysis, *Adv. Funct. Mater.* 29 (2019) 1900704.
- [65] J.S. Yoo, X.i. Rong, Y. Liu, A.M. Kolpak, Role of lattice oxygen participation in understanding trends in the oxygen evolution reaction on perovskites, *ACS Catal.* 8 (5) (2018) 4628–4636.
- [66] Z.-F. Huang, J. Song, Y. Du, S. Xi, S. Dou, J.M.V. Nsanzimana, C. Wang, Z.J. Xu, X. Wang, Chemical and structural origin of lattice oxygen oxidation in Co–Zn oxyhydroxide oxygen evolution electrocatalysts, *Nat Energy* 4 (4) (2019) 329–338.
- [67] Y.L. Zhu, H.A. Tahini, Z.W. Hu, Z.G. Chen, W. Zhou, A.C. Komarek, Q. Lin, H.J. Lin, C.T. Chen, Y.J. Zhong, M.T. Fernandez-Díaz, S.C. Smith, H.T. Wang, M.L. Liu, Z. P. Shao, Boosting oxygen evolution reaction by creating both metal ion and lattice-oxygen active sites in a complex oxide, *Adv. Mater.* 32 (2020) 1905025.
- [68] X. Wang, Z. Pan, X. Chu, K. Huang, Y. Cong, R. Cao, R. Sarangi, L. Li, G. Li, S. Feng, Atomic-scale insights into surface lattice oxygen activation at the spinel/perovskite interface of  $\text{Co}_3\text{O}_4/\text{La}_{0.3}\text{Sr}_{0.7}\text{CoO}_3$ , *Angew. Chem. Int. Ed.* 58 (34) (2019) 11720–11725.
- [69] J.T. Mefford, X. Rong, A.M. Abakumov, W.G. Hardin, S. Dai, A.M. Kolpak, K. P. Johnston, K.J. Stevenson, Water electrolysis on  $\text{La}_{1-x}\text{Sr}_x\text{CoO}_{3-\delta}$  perovskite electrocatalysts, *Nat. Commun.* 7 (2016) 11053.
- [70] Y.L. Zhu, Q. Lin, Z.W. Hu, Y.B. Chen, Y.C. Yin, H.A. Tahini, H.J. Lin, C.T. Chen, X. W. Zhang, Z.P. Shao, H.T. Wang, Self-assembled Ruddlesden-Popper/perovskite hybrid with lattice-oxygen activation as a superior oxygen evolution electrocatalyst, *Small* 16 (2020) 2001204.